The response to pulse-like perturbations in atmospheric carbon and carbon isotopes

Aurich Jeltsch-Thömmes and Fortunat Joos

Climate and Environmental Physics, Physics Institute and Oeschger Centre for Climate Change Research, University of Bern, Bern, Switzerland

Correspondence: Aurich Jeltsch-Thömmes (jeltsch@climate.unibe.ch)

Abstract. Measurements of carbon isotope variations in climate archives and isotope-enabled climate modelling foster the understanding of the carbon cycle. Perturbations in atmospheric CO_2, and in its isotopic ratios ($\delta^{13}C$, $\Delta^{14}C$) are removed on different time scales and by partly different processes. We investigate these differences on timescales of up to 100,000 years in idealized pulse release experiments with the Bern3D-LPX Earth system model of intermediate complexity and by analytical solutions from a box model. Isotopic perturbations are initially removed much faster from the atmosphere than perturbations in CO_2 as explained by aquatic carbonate chemistry. On longer time scales, the CO_2 perturbation is removed by carbonate compensation and silicate rock weathering. In contrast, the $\delta^{13}C$ perturbation is removed by the relentless flux of organic and calcium carbonate particles buried in sediments. The associated removal rate is significantly modified by spatial $\delta^{13}C$ gradients within the ocean influencing the isotopic perturbation of the burial flux. Space-time variations in ocean $\delta^{13}C$ perturbations are captured by three Principal Components and Empirical Orthogonal Functions. Analytical impulse response functions for atmospheric CO_2 and $\delta^{13}CO_2$ are provided. Our results show that changes in terrestrial carbon storage are unlikely the sole cause for the abrupt, centennial CO_2 and $\delta^{13}C$ variations recorded in ice during Heinrich Stadials HS1 and HS4 of the last glacial period. Ocean processes likely played a significant role. The $\delta^{13}C$ offset between the penultimate and last glacial maximum reconstructed for the ocean and atmosphere is most likely caused by imbalances between weathering, volcanism and burial fluxes.

1 Introduction

Research efforts to understand the past and future evolution of atmospheric CO_2 and of its isotopic signature are ongoing since many decades. Yet, open questions still remain, such as the mechanisms governing glacial-interglacial CO_2 variations over the past 800 thousand years recorded in ice cores (e.g. Neftel et al., 1982; Siegenthaler et al., 2005; Lüthi et al., 2008; Marcott et al., 2014; Bereiter et al., 2015). Or more specifically, to the offsets in the stable isotope signature of CO_2 ($\delta^{13}C_{atm}$) and of dissolved inorganic carbon ($\delta^{13}C_{DIC}$) between the Penultimate (PGM) and Last Glacial Maximum (LGM) and between the two recent interglacials, the Eem and and the Holocene (Schneider et al., 2013; Eggleston et al., 2016; Hoogakker et al., 2006; Oliver et al., 2010). Could this PGM-LGM $\delta^{13}C$ offset result from a change in terrestrial carbon storage, or rather from changes in carbon and carbon isotope fluxes connected to the sedimentary weathering-burial cycle? Further questions remain regarding

CO_2 and $\delta^{13}C_{atm}$ variations on centennial and millennial timescales and a possible role of changes in the land biosphere carbon inventory (e.g. Köhler et al., 2010; Skinner et al., 2010; Schmitt et al., 2012; Skinner et al., 2017; Bauska et al., 2018). Reconstructed variations in CO_2 and $\delta^{13}C_{atm}$ during Heinrich Stadial (HS) 4 and 1, two northern hemisphere cold periods during the last glacial, have been attributed to changes in terrestrial carbon storage (e.g. Bauska et al., 2016, 2018).

5   The perturbations in CO_2 and $\delta^{13}CO_2$ due to a carbon input (or removal) from the land biosphere or from fossil fuel burning are removed by a few principal processes. In the case of CO_2, over the first decades and centuries, it is ocean invasion and land uptake, on millennial timescales $CaCO_3$ compensation, and finally, on timescales of hundreds of thousands of years the remaining atmospheric CO_2 perturbation is removed by enhanced silicate rock weathering (e.g. Archer et al., 1998; Joos et al., 2001, 2013; Colbourn et al., 2015; Lord et al., 2015). In the case of $\delta^{13}C$, the perturbation is mixed rather quickly throughout

10   the atmosphere-land-ocean reservoir and is removed on multi-millennial timescales by changes in the isotopic signature of weathering and burial fluxes.

Simulations of climate and CO_2 over thousands of years with dynamic, 3-dimensional models remain still challenging. Over the last decades, computational power has continuously increased and first results from simulations with Earth System Models of Intermediate Complexity (EMICs) covering glacial-interglacial cycles have been published (e.g. Brovkin et al., 2012;

15   Menviel et al., 2012; Ganopolski and Brovkin, 2017). However, to date these long timescales prevented large ensemble simulations with spatially resolved models as well as glacial-interglacial simulations using state-of-the-art Earth System Models. A possible tool to overcome these computational obstacles is the use of reduced form models invoking Impulse Response Functions (IRFs) and Principal Component - Empirical Orthogonal Function (PC-EOF) analysis. IRFs and PC-EOF analysis are instrumental to characterize the fundamental time and spatial scales of model response to a perturbation.

20   The response of a linear system to a perturbation such as carbon emissions to the atmosphere can be fully characterized by its IRF. The atmosphere-ocean CO_2 cycle can be approximated as a nearly linear system, as long as concentrations do not vary much, i.e. less than a doubling of pre-industrial CO_2 concentrations (Hooss et al., 2001). The perturbation in the atmosphere or ocean is then given by the convolution integral of the emission history and the corresponding IRF (e.g. Joos and Bruno, 1996; Joos et al., 1996). IRFs can easily be described by a sum of exponentials, yielding a cost efficient substitute model for

25   describing the temporal evolution of an atmospheric CO_2 perturbation. IRFs have been widely used to calculate remaining atmospheric fractions of anthropogenic CO_2 emissions on different timescales and to characterize model behaviour and their characteristic response time scales (e.g. Siegenthaler and Oeschger, 1978; Maier-Reimer and Hasselmann, 1987; Sarmiento et al., 1992; Siegenthaler and Joos, 1992; Enting et al., 1994; Joos and Bruno, 1996; Archer et al., 1997, 1998; Ridgwell and Hargreaves, 2007; Archer and Brovkin, 2008; Archer et al., 2009; Joos et al., 2013; Colbourn et al., 2015; Lord et al., 2015).

30   However, peer-reviewed studies that quantify the IRF for carbon isotopes of CO_2 are scarce (Schimel et al., 1996; Joos and Bruno, 1996) and, to our knowledge, not available for multi-millennial time scales.

Principal Component analysis is widely used to capture the information of multi-dimensional data. The atmospheric perturbation in CO_2 and its isotopes in response to carbon input external to the ocean-atmosphere system is propagated to the ocean. The resulting spatio-temporal (4-D) evolution of marine tracers may be conveniently approximated using PC-EOF analysis.

35   The perturbation is described as a superposition of spatial empirical orthogonal functions ($EOF(\boldsymbol{x})$) multiplied with the corre-

sponding time dependent principal component (PC(t)). Combining IRF and PC-EOF then allows to compute the perturbation in space and time with minimal computational resources (Hooss et al., 2001; Joos et al., 2001)

The main goal of this study is to investigate the time scales and underlying processes for the removal of an atmospheric perturbation in CO_2 and its $\delta^{13}C$ signature in response to an external carbon input. To this end, we performed pulse-release

5　(uptake) experiments over 100,000 years with the Bern3D-LPX EMIC. We determine characteristic Impulse Response (or Green's) Functions (IRF) and describe marine spatio-temporal variations using PC-EOF analysis. Responses in atmospheric radiocarbon signature ($\Delta^{14}C$) are briefly addressed. Implications of our results for the PGM-LGM $\delta^{13}C$ difference and for past centennial CO_2 variations are discussed. Simple expressions that illuminate the fundamental differences in the removal time scales for an atmospheric perturbation in CO_2 versus the associated perturbation in $\delta^{13}CO_2$ are developed in the Appendix. The

10　pulse experiments are thought to represent (i) the sudden carbon uptake from or release to the atmosphere by the land biosphere, (ii) the release of old organic carbon, e.g., from ancient peat or permafrost material, (iii) the burning of all conventional fossil fuel resources, and (iv) a variation in ^{14}C production by cosmic radiation or atomic bomb tests.

2　Model and experimental set-up

2.1　The Bern3D-LPX model

15　For this study, the Bern3D v2.0s Earth System Model of Intermediate Complexity (EMIC) is used coupled to the dynamic vegetation model LPX-Bern v1.4. The Bern3D consists of a three dimensional geostrophic ocean (Edwards et al., 1998; Müller et al., 2006) with an isopycnal diffusion scheme and Gent-Mc Williams parameterization for eddy-induced transport (Griffies, 1998), a single layer energy-moisture balance atmosphere to which a thermodynamic sea-ice component is coupled (Ritz et al., 2011). We use the ocean model coupled to a 10 layer sediment module (Tschumi et al., 2011; Heinze et al., 1999) with updated

20　sediment parameters (Jeltsch-Thömmes et al., 2019) and to a global representation of rock weathering (Colbourn et al., 2013). The resolution of the Bern3D model components is 41x40 horizontal grid cells with 32 logarithmically spaced depth layers in the ocean. Wind stress at the ocean surface is prescribed from the NCEP/NCAR monthly wind stress climatology (Kalnay et al., 1996) and air-sea gas exchange and carbonate chemistry follow OCMIP-2 protocols (Najjar and Orr, 1999; Orr et al., 1999; Wanninkhof, 2014; Orr and Epitalon, 2015; Orr et al., 2017). The global mean air-sea gas transfer rate is reduced by 19

25　% to match observational radiocarbon estimates (Müller et al., 2006) and gas transfer velocity scales linearly with wind speed (Krakauer et al., 2006).

Marine productivity is calculated as a function of light availability, temperature, and nutrient concentrations (P, Fe, Si), and is restricted to the euphotic zone in the uppermost 75 m. Tracers, including dissolved inorganic carbon and semi-labile organic carbon (DIC, DOC), the corresponding isotopic forms, as well as alkalinity (Alk), phosphate (PO_4), oxygen (O_2), iron

30　(Fe), silica (Si), and an ideal age tracer, are transported by advection, diffusion, and convection. Biogeochemical cycling is described in detail in Tschumi et al. (2011) and Parekh et al. (2008) and subsequent studies (e.g. Menviel and Joos, 2012; Menviel et al., 2012; Roth and Joos, 2012; Roth et al., 2014; Menviel et al., 2015; Battaglia et al., 2016; Battaglia and Joos,

2018a, b; Jeltsch-Thömmes et al., 2019). Isotopic fractionation between model components is documented in Jeltsch-Thömmes et al. (2019).

The sediment module dynamically calculates the transport, redissolution/remineralization, and bioturbation of solid material, the pore water chemistry, and diffusion in the top 10 cm of the sediment. Four solid tracers ($CaCO_3$, opal, POC, clay) and seven

5 tracers in the porewater (DIC, $DI^{13}C$, $DI^{14}C$, alkalinity, phosphate, oxygen, and silicic acid) are modeled. The dissolution of $CaCO_3$ and POC depends on the respective weight fraction of $CaCO_3$ and POC in the solid phase of the sediment and the pore-water CO_3^{2-} and O_2 concentration, respectively. Denitrification is not considered in this model version, but O_2 is not consumed below a threshold, somewhat reflecting the process of denitrification without modeling NO_3^-. The respective reaction rate parameters for $CaCO_3$ dissolution and POC oxidation are global constants (see Roth et al., 2014; Jeltsch-Thömmes et al.,

10 2019). The model assumes conservation of volume, i.e. the entire column of the sediments is pushed downward if deposition exceeds redissolution into pore waters. Any solid material that is pushed out of the diagenetic zone (top 10 cm) disappears into the subjacent diagenetically consolidated zone (burial or loss flux) (see Tschumi et al., 2011, for more details). Carbonate chemistry within sediment pore waters is calculated as in the ocean by using the MOCSY routine of Orr and Epitalon (2015).

Weathering fluxes of PO_4, Alk, DIC, $DI^{13}C$, and silicic acid are added uniformly to the coastal surface ocean. The global

15 weathering fluxes are set equal to the burial fluxes diagnosed at the end of the model spin-up. The isotopic signature of the weathering carbon corresponds to the respective signature of the burial fluxes and amounts to $\delta^{13}C$ = -9.2 ‰, intermediate between isotopically light organic carbon ($\delta^{13}C$ = -20.5 ‰) and heavier $CaCO_3$ ($\delta^{13}C$ = 2.9 ‰). During experiments, weathering fluxes of $CaCO_3$ and $CaSiO_3$, and accordingly DIC, $DI^{13}C$, and alkalinity, are allowed to vary as a function of surface air temperature, runoff, and net primary productivity (NPP). The parameterization of this weathering feedback follows equations

20 described in detail in Colbourn et al. (2013). The runoff dependence is parameterized as a function of temperature and for the productivity feedback the NPP from the coupled LPX-Bern model is used. We apply weathering feedbacks in the global average 0-D version (Colbourn et al., 2013, 2015).

The Bern3D model is coupled to the Land surface Processes and eXchanges (LPX) model v1.4 (Lienert and Joos, 2018) which is based on the Lund-Potsdam-Jena (LPJ) model (Sitch et al., 2003). In LPX, coupled nitrogen, water, and carbon cy-

25 cles are simulated and vegetation composition is determined dynamically and represented with 20 (15 on natural and 5 on anthropogenically used land) plant functional types (PFTs). The PFTs compete within their bioclimatic limits for resources. CO_2 assimilation of plants is implemented following Farquhar et al. (1980) and Haxeltine and Prentice (1996a, b) and isotopic discrimination during photosynthesis is calculated according to Lloyd and Farquhar (1994). The carbon cycles of Bern3D and LPX-Bern are coupled through carbon and isotope exchange fluxes between the land and atmosphere and between the

30 ocean and atmosphere. Climate change information from the Bern3D is passed on to LPX-Bern via a pattern scaling approach (Stocker et al., 2013). Spatial anomaly patterns in monthly temperature and precipitation, derived from a 21st century simulation with the Community Climate System Model (CCSM4), are scaled by the anomaly in global monthly mean surface air temperature as computed interactively by the Bern3D. These anomaly fields are added to the monthly baseline (1901 to 1931 AD) climatology of the Climate Research Unit (CRU) (Harris et al., 2014). A more detailed description of the LPX-Bern model

35 can be found in Keller et al. (2017) and Lienert and Joos (2018).

2.2 Experimental protocol

The Bern3D model is spun-up over 60 thousand years (kyrs) to a pre-industrial steady state with 1850 AD boundary conditions. Atmospheric CO_2 is prescribed to 284.7 ppm, $\delta^{13}C$ to -6.305 ‰, and $\Delta^{14}C$ to 0 ‰. For LPX, the land area under anthropogenic use is fixed to its 1850 AD extent and kept constant in all simulations. The LPX-Bern model is spun-up uncoupled under
5   identical 1850 AD boundary conditions over 2,500 years. Bern3D and LPX-Bern are then coupled and equilibrated for 500 years, again under fixed 1850 AD boundary conditions. After the spin-up, atmospheric CO_2 and its isotopic ratio are calculated interactively, with enabled carbon–climate feedbacks. Pulse experiments are started from the 1850 AD equilibrium state at nominal year -100. After 100 years, i.e., during nominal year 0 of the simulations, an external flux of carbon with characteristic isotopic signatures is removed from or added to the model atmosphere at a constant rate over the year. Runs are continued for
10 100 kyrs to simulate the redistribution of the added carbon and isotopes in the Earth system.

Table 1 summarizes run names and key characteristics of all simulations. Pulse sizes are varied between -250 GtC (removal) to +500 GtC (addition) with $\delta^{13}C$ of -24 ‰ and $\Delta^{14}C$ of 0 ‰ . This corresponds to a hypothetical, sudden uptake or release of carbon from the land biosphere with a typical C3-like $\delta^{13}C$ signature. For simplicity and to ease interpretation, we set the $\Delta^{14}C$ of these land biosphere carbon pulses to the atmospheric signature; thus, we assume that the released material has been
15 recently assimilated and neglect the small depletion in ^{14}C of "young" plant, litter, and soil material. In sensitivity experiments, $\Delta^{14}C$ is set to -500 ‰ and -1,000 ‰ to mimic the release of old, dead organic carbon, for example from buried peat or permafrost soils instead of young plant-derived material. In another simulation, the isotopic signatures are set to the signature for the modern mix of fossil fuels. Finally, we also performed a run where only ^{14}C, but no ^{12}C and ^{13}C is added to represent a change in radiocarbon production in the atmosphere. All these simulations were performed with fully interactive ocean
20 sediments and enabled $CaCO_3$ and $CaSiO_3$ weathering feedbacks. The influence of the weathering feedback and of ocean-sediment interactions is quantified using two additional simulations. First, the weathering input flux is kept time invariant ("no weathering feedback"), Second, the sediment module is, in addition, not included in a so-called "closed" atmosphere-ocean-land model setup.

2.3 Data reduction

25 The remaining fraction of a pulse-like perturbation or IRF at time t after the pulse release is defined for atmospheric CO_2 as

$$\text{IRF}(CO_{2,a})(t) = \frac{\Delta CO_{2,a}(t)}{\Delta CO_{2,a}^{ini}} = \frac{CO_{2,a}(t) - CO_{2,a}^{ctrl}(t)}{P/\left(2.12 \text{ GtC ppm}^{-1}\right)}. \tag{1}$$

Δ indicates a perturbation, here evaluated as difference between a simulation with pulse release and a corresponding control simulation. P indicates the pulse size in GtC which yields the initial atmospheric CO_2 perturbation in ppm when divided by 2.12 GtC ppm^{-1}. The superscript $ctrl$ refers to the control simulation without pulse, ini to the (maximum) initial perturbation
30 assuming an instantaneous carbon release, and subscript a to the atmosphere. The IRF for $\delta^{13}C_a$ is:

$$\text{IRF}(\delta^{13}C_a)(t) = \frac{\delta^{13}C_a(t) - \delta^{13}C_a^{ctrl}(t)}{\Delta \delta^{13}C_a^{ini}}. \tag{2}$$

Table 1. Overview of simulations

Run name	Pulse size	δ^{13}C	Δ^{14}C	model setup
	(GtC)	(‰)	(‰)	
$ctrl$	0	–	–	std.
land biosphere C source				
$n250$	-250	-24	0	std.
$n100$	-100	-24	0	std.
$p100$	100	-24	0	std.
$p250$	250	-24	0	std.
$p500$	500	-24	0	std.
old organic C source (old soils / fossil fuels)				
$^{14}C_{-500}$	100	-24	-500	std.
$^{14}C_{dead}$	100	-24	-1000	std.
$p5000$	5000	-28	-1000	std.
radiocarbon production anomaly				
$^{14}C_{only}$	–	–	(100 GtC $\times$ $^{14}\mathbf{R}_{std})^{a}$	std.
sensitivity to model setup				
SED_{500}	500	-24	0	no wea.[b]
SED_{ctrl}	0	–	–	no wea.[b]
CLO_{500}	500	-24	0	closed[c]
CLO_{ctrl}	0	–	–	closed[c]

[a]The number of ^{14}C atoms corresponding to 100 GtC of carbon with
Δ^{14}C=0 ‰ is added.

[b] Setup without $CaCO_3$ and $CaSiO_3$ weathering feedbacks.

[c]"Closed system": atm-ocean-land without ocean sediment module
and $CaCO_3$ and $CaSiO_3$ weathering feedbacks.

$\Delta\delta^{13}\mathrm{C}_a^{ini}$ denotes the initial isotopic perturbation in the atmosphere and equals:

$$\Delta\delta^{13}\mathrm{C}_a^{ini} = \frac{P}{N_{a,0} + P} \cdot (\delta^{13}\mathrm{C}_P - \delta^{13}\mathrm{C}_{a,0}). \tag{3}$$

$\delta^{13}\mathrm{C}_P$ indicates the isotopic signature of the pulse, the subscript 0 the value prior to the pulse, and N_a the atmospheric carbon inventory. Analogous equations to Eqs. 2 and 3 hold for $\Delta^{14}\mathrm{C}$.

5   An analytical expression for the IRF is calculated from experiment $p500$. The IRF is fitted by the sum of five exponential terms to

$$\mathrm{IRF}(\mathrm{CO}_{2,a}(t)) = a_0 + \sum_{i=1}^{5} a_i \cdot exp\left(\frac{-t}{\tau_i}\right) \; for \; t \geq 0 \tag{4}$$

using a least-squares optimization routine in Python. The coefficients a_i are fractions of the perturbation, each associated with a timescale τ_i, and a_0 the fraction of the perturbation remaining constantly in the atmosphere ($\tau_0 = \infty$). The sum over all

10 six coefficients a_i equals 1. Modeled values are well reproduced with n=5 exponents. Differences between the original model output and the fit are insignificant for practical applications. Finally, we note that the IRF or remaining atmospheric fraction is in our experimental setup always smaller than one: the carbon is added at a constant rate during year 0 in the pulse simulations and part of this carbon is already taken up by the ocean during this initial year. Similarly, the IRF for $\delta^{13}\mathrm{C}_a$ is fitted with n=4 exponents.

15   Principal component empirical orthogonal function (PC-EOF) analysis is used to fit the $^{13}\mathrm{C}$ isotopic perturbations of dissolved inorganic carbon (DIC) in the ocean ($\Delta\delta^{13}\mathrm{C}_{\mathrm{DIC}}$). To this mean, the Python package $eofs$ (Dawson, 2016) is used to calculate principal component timeseries ($\mathrm{PC}(t)$) and the spatial empirical orthogonal functions ($\mathrm{EOF}(\boldsymbol{x})$) from the volume-weighted 4-D field of $\Delta\delta^{13}\mathrm{C}_{\mathrm{DIC}}(t,\boldsymbol{x})$. PCs and EOFs are then used to build a cost-efficient substitute model of the spatio-temporal evolution of $\Delta\delta^{13}\mathrm{C}_{\mathrm{DIC}}$ in response to an atmospheric pulse perturbation. The output frequency for marine 3-D tracer

20 fields after the perturbation is every 10 years during the first 1 kyr, every 200 years until 10 kyrs and every 1 kyr thereafter. In the PC-EOF calculation this gives more weight to the first part of the simulation, where changes in the perturbation are larger.

2.4   Results

2.5   Earth system response to a pulse release of carbon

Impulse response functions for atmospheric CO$_2$ and δ^{13}C: We first describe the IRF for the atmospheric CO$_2$ perturbation

25 using experiment $p250$ (Fig. 1a). The initial spike in response to the carbon release is followed by a substantial decline over the first decades due to carbon uptake by the upper ocean and land biosphere. The IRF is reduced to less than 40 % within the first century and decreases further on the timescale of ocean mixing to less than 16 % by year 2,000. The fit by exponentials (Table 2) yields time scales of 6, 47, and 362 years for this initial decline. They represent the continuum of carbon overturning time scales within the ocean and the land biosphere as well as time scales governing air-sea and air-land carbon exchange.

30   CaCO$_3$ compensation and weathering-burial imbalances remove the atmospheric perturbation on multi-millennial timescales such that after 10 kyrs less than 8 % and after 100 kyrs less than 2 % of the CO$_2$ perturbation remain airborne (Fig. 1a). The
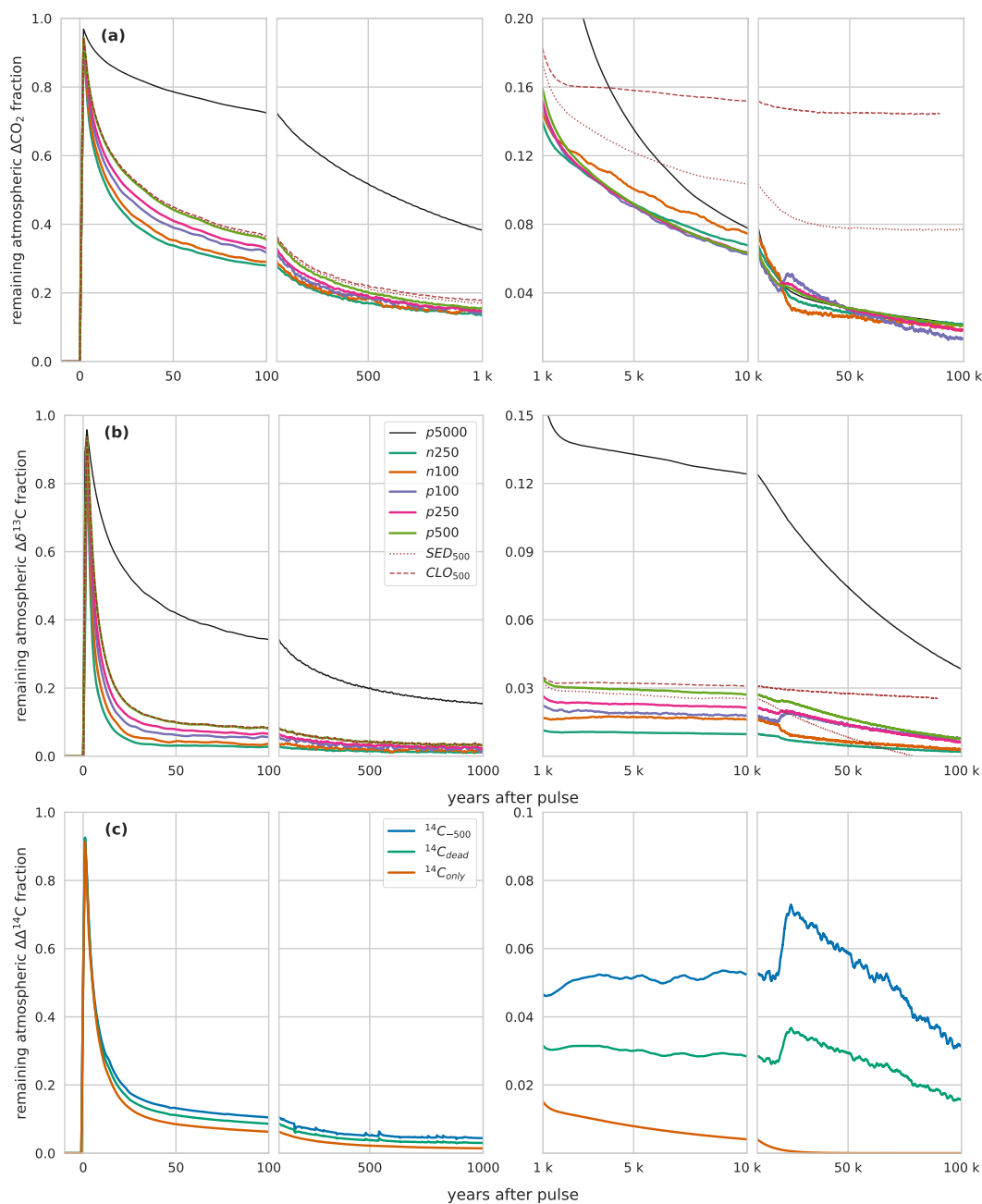
Climate
of the Past
Discussions

Open Access

Figure 1. (a) CO₂,(b) δ^{13}C, and (c) Δ^{14}C perturbation in the atmosphere for different simulations with different pulse sizes and model configurations. The isotopic signature is δ^{13}C=-24 ‰ for all pulse sizes except the 5000 GtC pulse with δ^{13}C=-28 ‰. Dashed and dotted brown lines in panel (a) and (b) show results from a 500 GtC pulse with no weathering feedback and no ocean sediments, respectively. See Table 1 and section 2.2 for details of the experimental setup of the runs. Note that the scaling of the second y-axis is different for the three panels. Data are filtered with a moving average of 1000 years in the interval 1 kyr - 100 kyrs for better visibility. Note that experiment CLO_{500} was run for 90 instead of 100 kyrs.

Table 2. Fit parameters for $IRF(\Delta CO_2(t))$ and $IRF(\Delta\delta^{13}C_a(t))$ of $p500$.

	CO_2		$\delta^{13}C_a$	
i	a_i	τ_i (yrs)	a_i	τ_i (yrs)
0	0.008	-	0.001	-
1	0.044	68,521	0.034	74,781
2	0.112	5,312	0.034	436
3	0.224	362	0.092	75
4	0.310	47	0.840	6
5	0.297	6		

fit by exponentials shows that a fraction of 11.2 % of the initial perturbation is removed with a time scale of 5.5 kyrs. We associate these values with the process of $CaCO_3$ compensation. A remaining fraction of 4 to 5 % is removed with a time scale of 69 kyrs (Table 2), linked to enhanced silicate rock weathering. The jumps visible at around 20 kyrs in Fig. 1 arise from a sea ice-albedo feedback in the control run and are thus most pronounced in the experiments with smaller perturbations. These

5   jumps are not of further relevance for our discussion.

Compared to CO_2, the atmospheric $\delta^{13}C$ perturbation is initially removed much faster (Fig. 1b). Within the first decades, $IRF(\delta^{13}C_a)$ is reduced to below 10 %. The further decline is slower and 1 kyr after the pulse, less than 3 % of the initial perturbation remains airborne. The remaining atmospheric perturbation is finally reduced to ≤ 1 % of the initial perturbation at the end of the simulation (Fig.1b). The fit by exponentials for $IRF(\delta^{13}C_a)$ (Table 2) shows that 84 % of the perturbation are

10   removed with a timescale of 6 years, reflecting the initial fast decline seen in Fig. 1b when the perturbation is mixed in the upper ocean and living vegetation. About 9 % and 3 % are removed on timescales of 75 and 436 years, respectively, reflecting the decadal and centennial mixing of the perturbation in the land biosphere and deeper ocean. $\sim$3 % of the perturbation are finally removed with a timescale of $\sim$74 kyrs, in agreement with the e-folding timescale of the decline ($\sim$70 kyrs; see further below). However, it has to be kept in mind, that these removal timescales result from a fit and thus several, different solutions

15   are possible.

Processes: Next, we address the processes behind the different temporal evolution of $CO_{2,a}$ and $\delta^{13}C_a$. We focus on the ocean as ocean uptake is thought to dominate on long time scales. A perturbation in atmospheric CO_2 or in $^{13}CO_2$ is communicated by air-sea gas exchange to the surface ocean and further transported, mainly by physical processes, to the deep ocean. The fundamental difference between the IRF for $CO_{2,a}$ and $\delta13C_a$ is linked to the aquatic carbonate chemistry and the

20   associated equilibrium between dissolved CO_2, bicarbonate and carbonate ions ($CO_2 + H_2O \Leftrightarrow HCO_3^- + H^+ \Leftrightarrow CO_3^{2-} + 2H^+$) (Dickson et al., 2007). The removal of an atmospheric CO_2 perturbation is co-controlled by this acid-base carbonate chemistry (Revelle and Suess, 1957). In contrast, the removal of a perturbation in the isotopic ratio $^{13}CO_2/^{12}CO_2$ is hardly affected by this chemical buffering, because $^{13}CO_2$ and $^{12}CO_2$ are affected approximately equally by the acid-base chemistry reactions. The chemical buffering diminishes the uptake capacity of the ocean for CO_2, but not for the isotopic ratio. Correspondingly, the

IRF for $CO_{2,a}$ decreases less rapidly than the IRF for $\delta^{13}C_a$ and IRF($\delta^{13}C_a$) is smaller than IRF($CO_{2,a}$) over the simulation period.

For an illustrative, semi-quantitative analysis, we developed approximate expressions for the IRF for $CO_{2,a}$ and $\delta^{13}C_a$ for time scales up to 2 kyrs as explained in the Appendix. Simplifying assumptions are that equilibrium between the atmosphere

5 and a fraction of the ocean with the initial carbon inventory $N_{o,0}$ is assumed, while land biosphere carbon uptake and other climate-carbon cycle feedbacks are neglected. For CO_2 the expressions reads:

$$\text{IRF}_\infty(\text{CO}_{2,a}) = \frac{N_{a,0}}{N_{a,0} + \frac{1}{\xi}N_{o,0}}, \quad \text{for } 0 \le t \le 2 \text{ kyrs}, \tag{5}$$

The subscript a indicates the atmosphere and o the ocean, 0 the time prior to the pulse and ∞ the time when an effective ocean volume with the initial carbon inventory $N_{o,0}$ is equilibrated with the atmosphere, P denotes again the pulse size. ξ is the

10 oceanic buffer or Revelle Factor. ξ describes the influence of the acid-base carbonate chemistry on the relationship between the relative perturbation in the CO_2 partial pressure and in dissolved inorganic carbon (DIC) (Revelle and Suess, 1957). ξ varies with environmental conditions and is on the order of 10. The key information of eq. 5 is that the magnitude of the IRF is determined by the ratio of the (equilibrated) ocean carbon inventory and the buffer factor, $N_{o,0}/\xi$. The smaller this ratio, the larger is IRF($CO_{2,a}$).

15 For $\delta^{13}C_a$, we also consider the initial carbon inventory of the land biosphere ($N_{b,0}$) and develop a corresponding expression (for the derivation see the Appendix):

$$\text{IRF}_\infty(\delta^{13}C_a) = \frac{N_{a,0} + P}{N_{a,0} + N_{o,0} + N_{b,0} + P} \cdot \frac{(\delta^{13}C_P - \delta^{13}C_{mean})}{(\delta^{13}C_P - \delta^{13}C_{a,0})}, \quad \text{for } 0 \le t \le 2 \text{ kyrs} \tag{6}$$

Equation 6 shows that IRF($\delta^{13}C_a$) is described by the product of two ratios. The first ratio corresponds to the ratio of the carbon inventory in the atmosphere immediately after the pulse release to the total carbon inventory in the ("equilibrated")

20 atmosphere-ocean-land biosphere system. It tells us that the pulse perturbation is mixed uniformly (see also Appendix eq. A20) and in proportion to the carbon inventories of the different reservoirs atmosphere, ocean, land biosphere. The second fraction is about 1.2 and thus a correction term of order 20 % for small pulses sizes as typically applied in this study. It arises as the isotopic signature of the ocean and land biosphere is different from that of the atmosphere. $\delta^{13}C_{mean}$ corresponds to the weighted mean signature of the atmosphere, ocean and land biosphere, with the fraction of the pulse found in each of these

25 reservoirs as weights (Appendix eq. A27). Remarkably, the buffer factor ξ does not directly show up in eq. 6. The reason is, as noted already above, that CO_2 and $^{13}CO_2$ are both about equally affected by the aquatic chemistry. In turn, their ratio, i.e., $\delta^{13}C$, is hardly affected by this acid-base buffering.

Equation 5 and eq. 6 reveal the fundamental difference between a perturbation in CO_2 (and $^{13}CO_2$) and in the isotopic ratio, $\delta^{13}CO_2$. For small pulse sizes ($P \to 0$), neglecting the influence of the land biosphere and the correction term in eq. 6 for $\delta^{13}C$,

30 eq. 6 and eq. 5 are formally equal, except that a buffer factor ξ of 1, instead of $\sim$12 applies for $\delta^{13}C_a$. Eqs. 6 and 5 show: the pulse perturbation is distributed between the atmosphere and ocean proportionally to their initial carbon inventories $N_{a,0}$ and $N_{o,0}$ in the case of $\delta^{13}C_a$, but proportionally to $N_{a,0}$ and $N_{o,0}/\xi$ in the case of CO_2. As a consequence, the perturbation in the

ratio $\delta^{13}C_a$ is apparently removed much fast than the perturbation in the concentration $CO_{2,a}$, despite that the time scales to transport a perturbation from the surface ocean to the deep ocean by advection, convection, and diffusion are the same.

We may illustrate this difference in the removal rate numerically. ξ is about 12, $N_{a,0}$ is 600 GtC, $N_{o,0}$ is 37,400 GtC for the whole ocean. Further, the top 300 m with a carbon inventory of $\sim$2,600 GtC are approximately ventilated within a decade.

5 Then, the evaluation of eq. 5 yields for a small pulse that around 73 % and 16 % of the initial CO_2 perturbation are still found in the atmosphere after about 10 years and 2 kyrs, respectively. Regarding $\delta^{13}C$, the corresponding fractions (eq. 6) are much smaller and 12 % to 31 % and 1 % to 3 % for small pulse sizes (-250 GtC to 500 GtC; see Appendix, text after eq. A14 for more details). We assume the perturbation to have mixed with 500 GtC and 2,700 GtC on land after 10 and 2 kyrs, respectively. These values are roughly in agreement with the values shown in Fig. 1a for pulse sizes of up to 500 GtC.

10 Turning to intermediate time scales ($t \leq 20$ kyrs), $CaCO_3$ compensation further reduces the atmospheric CO_2 perturbation and removes the differences in IRF($CO_{2,a}$) arising from different pulse sizes (Fig. 1a). The process of $CaCO_3$ compensation may be briefly explained as follows. CO_2 is taken up by the ocean and partly reacts to form bicarbonate (HCO_3^-) and hydrogen (H^+) ions. This makes the water more acidic; the carbonate ion concentration ($[CO_3^{2-}]$) is reduced and the water becomes corrosive to $CaCO_3$. In turn, sedimentary $CaCO_3$ dissolves to CO_3^{2-} and Ca^{2+} ions and less alkalinity and carbon, in the form

15 of $CaCO_3$, is buried in the litosphere than delivered by weathering input. Alkalinity and DIC concentrations adjust in response to the excess weathering, a so-called terrrestrial neutralization, and a new equilibrium between weathering and burial fluxes is established. This chain of processes raises the alkalinity twice as much as the DIC concentration in the ocean and additional CO_2 is taken up from the atmosphere.

Again, an approximate expression for the IRF($CO_{2,a}$) is developed. This applies for the time when $CaCO_3$ compensation
20 for the pulse perturbation is completed (see Appendix):

$$\text{IRF}_{CaCO_3}(CO_{2,a}) = 2 \cdot 1.5 \cdot \frac{N_{a,0}}{N_{o,0}}, \quad \text{for } t \sim 20 \text{ kyrs} \tag{7}$$

The factor 2 in eq. 7 arises from the acid-base carbonate chemistry, the factor 1.5 from the change in the ocean carbon inventory due to excess dissolution (or burial) of $CaCO_3$, equivalent to $\sim 0.5 \times P$. The factor 1.5 is model dependent (see e.g. Archer et al., 1998) and also slightly different from previous Bern3D model versions. This equation shows that the airborne
25 fraction depends on the ratio of the initial atmosphere ($N_{a,0}$) to ocean carbon inventory ($N_{o,0}$), when $CaCO_3$ compensation is completed. Therefore, IRF$_{CaCO_3}$ is (approximately) independent of the pulse size. Equation 7 successfully explains why IRF($CO_{2,a}$) for pulse sizes from -250 to +5,000 GtC take on a nearly identical value of 5 % around $\sim$20 kyrs after the pulse.

IRF($\delta^{13}C_a$) stays nearly constant between 1 and 10 kyrs (Fig. 1b). This implies that $CaCO_3$ compensation has little influence on the removal of the $\delta^{13}C$ perturbation. Reasons are that the change in ocean carbon inventory due to $CaCO_3$ dissolution
30 (burial) is small compared to the total ocean inventory and that the isotopic signature of $CaCO_3$ is similar to that of DIC.

On even longer time scales, the $CaSiO_3$ weathering feedback further removes the remaining perturbation in $CO_{2,a}$ with an e-folding time scale on the order of 70 kyrs. The perturbation in $\delta^{13}C_a$ is removed by the burial flux of organic carbon and $CaCO_3$. This burial flux removes the isotopic perturbation to the lithosphere. Surprisingly, the removal rate is substantially

faster than expected from the residence time of carbon and highly sensitive to the gradients in the perturbation of δ^{13}C ($\Delta\delta^{13}$C) within the ocean as further discussed below in the context of the factorial simulations and in the Appendix.

Factorial simulations: We now turn to the factorial simulations to further quantify the effect of $CaCO_3$ compensation, burial fluxes, and $CaCO_3$ and $CaSiO_3$ weathering feedbacks on the CO_2 and δ^{13}C perturbations. The evolution of IRF($CO_{2,a}$) for
5 experiment SED_{500} (no terrestrial weathering feedback but with marine sediments) is comparable to $p500$ until simulation year 1,000 and differs thereafter due to varying weathering rates in $p500$ (Fig. 1a). There is no additional addition of alkalinity to the ocean from enhanced terrestrial weathering in SED_{500} and $\Delta CO_{2,a}$ levels out at a higher value than in $p500$, with about 8 % of the perturbation remaining constantly airborne in SED_{500}. This value is in agreement with previous studies (e.g. Archer et al., 1998). It is somewhat higher than suggested by eq. 7 as this equation represents a simplification.

10 $CaCO_3$ compensation leads in both, $p500$ and SED_{500}, to a further removal of $\Delta CO_{2,a}$ on multi-millennial timescales as seen between 1 and 10 kyrs in Fig. 1a. After 10 kyrs, IRF($CO_{2,a}$) decreases further as a result of weathering-burial imbalances in the $CaCO_3$ flux, also referred to as terrestrial neutralization (e.g. Archer et al., 1998; Colbourn et al., 2015). The e-folding timescale for this terrestrial neutralization from SED_{500} is about 11 kyrs, higher than the value provided by Archer et al. (1998) (8.5 kyrs) but in the range (8 to 12 kyrs) provided by Colbourn et al. (2015).

15 Comparing $\Delta\delta^{13}C_{atm}$ of SED_{500} and $p500$, the evolution is initially comparable but on multi-millennial timescales the isotopic perturbation is, somewhat surprisingly and in contrast to the CO_2 perturbation, removed slower in $p500$ than in SED_{500}. In the case of SED_{500} the e-folding timescale is on the order of 20 to 30 kyrs. This is much shorter than expected from the mean residence time of carbon in the system of about 90 kyrs (Carbon inventory: ~40,000 GtC; burial flux: 0.46 GtC yr^{-1}). The long-term removal time scale is with about 70 kyrs also shorter than the residence time of carbon in simulation $p500$ with
20 enabled weathering feedbacks. The reason for the shorter e-folding timescale is apparent from Fig. 5g. The isotopic perturbation is larger in the surface ocean than in the ocean mean. In turn, the perturbation is removed more efficiently than expected from the residence time of carbon. The isotopic signature of the carbon burial flux is mainly determined by the upper ocean isotopic signature which is more depleted than the ocean mean for $p500$. In the case of SED_{500} this gradient is even stronger and the surface perturbation much larger than the ocean mean (not shown) (see section 2.6 for further explanation). These results
25 highlight the importance of spatial patterns within the ocean for the removal of an isotopic perturbation even for these very long-time scales. However, the absolute perturbation in $\delta^{13}C_a$ for these small pulse sizes and with δ^{13}C=-24 ‰ is rather small after a few kyrs. For example, in the case of SED_{500}, $\Delta\delta^{13}C_a$ decreases to below 0.05 ‰ after ~60 kyrs. The interannual variability from the LPX-Bern is of the same magnitude and also model drift starts to play a role.

Finally, we further exclude the effect of ocean sediment interactions and treat the atmosphere, ocean, and land biosphere as a
30 closed system in CLO_{500}. Considering ocean mixing times of 1-2 kyrs, we would expect the CO_2 perturbation for experiment CLO_{500} to reach a steady state within 2 kyrs. The slow response timescale of peat carbon in the LPX-Bern model, however, leads to a further decline of $\Delta CO_{2,a}$ over multiple millennia (Fig. 1a). About 15 % of the initial perturbation remain constantly airborne in the closed system model setting as expected from eq. 5. $\delta^{13}C_a$ levels out around 2 kyrs at around 3 ‰, as expected from eq. 6. The further decrease on multi-millennial timescales results from model drift in the LPX-Bern.
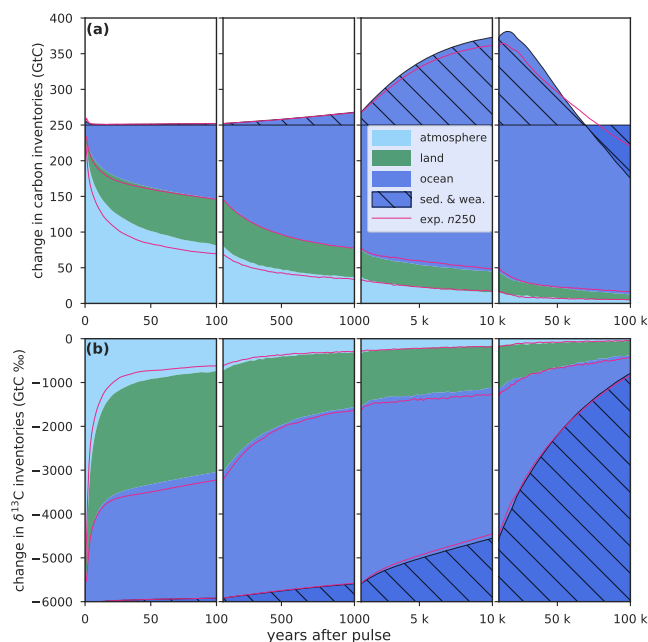
Figure 2. The budgets for the perturbations in (a) carbon and (b) $\delta^{13}C$ for experiment $p250$. Shown are inventories of the perturbations in the atmosphere (light blue), the land biosphere (green), and the ocean (blue). Hatched areas indicate the influence of changes in the lithosphere (including sediments) due to $CaCO_3$ compensation and imbalances in the weathering and burial fluxes on the carbon and isotopic inventories of the ocean-atmosphere-land system. For carbon, this inventory is elevated above the pulse perturbation of 250 GtC until about 70 kyrs and depleted thereafter. For $\delta^{13}C$, the atmosphere-ocean-land inventory is continuously reduced over the course of the simulation. Magenta lines show results for experiment $n250$ multiplied by -1.

The budgets of the carbon and carbon isotope perturbation: Next, we discuss the budgets of the carbon and ^{13}C perturbations for $p250$ (Fig. 2). After 100 years, about 82 GtC are still airborne and the land and the ocean carbon inventories have increased by about 65 GtC and 105 GtC, respectively (Fig. 2a). As time evolves, the oceanic carbon perturbation grows at the cost of the atmosphere and land. On multi-millennial timescales, carbonate compensation and enhanced terrestrial carbon-

5   ate and silicate weathering increase ocean alkalinity and thereby the uptake capacity for atmospheric CO_2 and the remaining atmospheric CO_2 fraction decreases. Nevertheless, the carbon perturbation in the atmosphere-ocean-land system exceeds the 250 GtC of the pulse as more carbon is added to the ocean through increased $CaCO_3$ weathering and redissolution/reduced burial of marine sediments (hatched area in Fig. 2a). The maximum perturbation is reached after ~16 kyrs with a total of about 381 GtC in the atmosphere-ocean-land system. Thereafter, this inventory decreases due to weathering-burial imbalances. After

10   100 kyrs, about 5 GtC of the perturbation remain airborne, 8 GtC are stored in the land biosphere, and the ocean contains 163 GtC more carbon than before the perturbation. Accordingly, 74 GtC of the initial perturbation are lost from the atmosphere-ocean-land system through increased marine burial compared to terrestrial weathering input (hatched area extends below 250 GtC line in Fig. 2a).

13

The isotopic budget is established by expressing any isotopic inventory by the product of the corresponding carbon inventory times its isotopic signature in units of $GtC\ ‰$. The role of the land biosphere in removing the $\delta^{13}C_a$ perturbation is clearly visible (Fig. 2b). After 100 years, the ocean contains $\sim$50 % of the isotopic perturbation (in $GtC\ ‰$), the land biosphere about 35 % and the atmosphere less than 15 %. On millennial timescales, the perturbation is slowly removed from the

5   atmosphere-ocean-land system. The $\delta^{13}C$ perturbation of the burial flux (combined POC and $CaCO_3$) follows the negative $\delta^{13}C$ perturbation in surface DIC. In turn, the burial flux mitigates the $\delta^{13}C$ perturbation from the atmosphere-ocean-land biosphere system (Fig. 2b).

Influence of pulse size: The IRF for atmospheric CO_2 and $\delta^{13}C$ is sensitive to the magnitude of the pulse size (Fig. 1a,b) and we next address related differences between simulations. For CO_2, the remaining atmospheric fraction is larger for larger

10   than for smaller pulse sizes. Differences are most pronounced in the first decades to centuries for small pulse sizes (-250 GtC to 500 GtC) and the first millennia for large pulse sizes ($p5000$; Fig. 1a). Several processes contribute to these differences.

First, non-linearities in the carbonate chemistry contribute to differences in IRF($CO_{2,a}$) in the first centuries to millennia, where the perturbation is largely contained in the atmosphere-ocean-land biosphere system. We see from eq. 5 that a controlling factor is the oceanic buffer factor. As pulse size increases so does the buffer factor, leading to higher values of IRF($CO_{2,a}$) for

15   $p5000$ compared to smaller pulse sizes (Fig. 1a).

Second, productivity on land depends non-linearly on CO_2 (Farquhar et al., 1980) and the loss of carbon from the land biosphere in response to a negative pulse is larger than the uptake in response to a positive pulse of same size. This contributes to the initially smaller remaining atmospheric fraction for negative pulses (see e.g., $p250$ and $n250$ in Fig. 1a and 2a). The difference is most strongly pronounced in the first centuries and millennia but prevails until the end of the simulation.

20   Third, also the response in marine export production is not linear for pulses of same absolute size but different sign. The initial decrease in export production after a positive pulse is smaller than the increase after a negative pulse of same size, thereby affecting surface ocean CO_2 concentrations and thus air–sea gas exchange and partly leveling out the effect from the land biosphere. For $\delta^{13}C_a$, the perturbation is smaller for negative than positive pulses of same absolute size (Fig. 1). The difference can be understood with the help of eq. 6. Evaluation of eq. 6 (see Appendix) yields an IRF($\delta^{13}C_a$) of $\sim$2 % for the

25   pulse addition of 250 GtC ($p250$), but of only $\sim$1 % for a corresponding removal ($n250$).

Radiocarbon: Finally, we discuss the $\Delta^{14}C$ perturbation experiments. In experiment $^{14}C_{only}$, a positive pulse of ^{14}C is added to the atmosphere but there is no perturbation in CO_2, analogous to a radiocarbon production pulse by atomic bomb tests or cosmic rays. The initial evolution of the IRF($\Delta^{14}C_a$) is very similar to the one of IRF($\delta^{13}C_a$) (Fig. 1b,c). On longer timescales, radioactive decay additionally removes the perturbation, so that after $\sim$20 kyrs less than 0.1 % of the perturbation is

30   left airborne. In simulations $^{14}C_{-500}$ and $^{14}C_{dead}$, a radiocarbon depleted carbon source of 100 GtC is added to the atmosphere causing a negative perturbation in $\Delta^{14}C$ and a positive perturbation in CO_2 in the atmosphere. As visible from Fig. 1a for $p100$, a small percentage of the CO_2 perturbation remains airborne even after 100 kyrs. This explains the persistence of a small atmospheric perturbation in $\Delta^{14}C$, well beyond the life time of the initially added ^{14}C. IRF($\Delta^{14}C_a$) is larger for $^{14}C_{-500}$ than for $^{14}C_{dead}$, as the initial perturbation in $\Delta^{14}C$ was smaller than for $^{14}C_{dead}$.

2.6 The δ^{13}C perturbation of marine dissolved inorganic carbon and its approximation by PC-EOF

The ocean mean perturbation in δ^{13}C of DIC ($\Delta\delta^{13}$C$_{DIC}$) increases in absolute magnitude during the first millennium, as the atmospheric perturbation is propagated to the ocean (Fig. 3, thick gray line). The most negative mean perturbation (-0.23 ‰ for experiment $p500$) occurs ∼1500 years after the pulse release (Fig. 3), reflecting ocean mixing timescales. Thereafter, the

5   δ^{13}C$_{DIC}$ perturbation decreases in magnitude as a result of weathering-burial imbalances (see section 2.5, Fig. 2 and 3). At the end of the simulation, less than 15 % of the maximum perturbation (-0.03 ‰) remain in the ocean.

Deep ocean invasion of the δ^{13}C$_{DIC}$ perturbation is first accomplished in the North Atlantic Deep Water (NADW) region. After 100 years, the signal has already propagated to a depth of∼3.5 km in the North Atlantic, whereas it is confined to the upper ocean (>1 km) in the rest of the ocean (Fig. 5a). At year 1,000, the δ^{13}C$_{DIC}$ perturbation is rather uniformly distributed in the

10   ocean. Only the deep North Pacific (region of oldest waters; ideal age >1 kyr in the Bern3D) and waters at intermediate depths in the Southern Ocean show a smaller perturbation (Fig. 5c). On multi-millennial times, $\Delta\delta^{13}$C$_{DIC}$ decreases throughout the ocean. The perturbation, however, is not entirely uniformly distributed as expected from a completed ocean mixing by physical transport. More negative $\Delta\delta^{13}$C$_{DIC}$ values are present in the upper ocean and in North Atlantic Deep Water than in the intermediate and deep Southern Ocean, in Antarctic Bottom Water in the Atlantic, and the deep Pacific (Fig. 5e,g).

15   Reasons behind are changes in the fractionation during air-sea gas exchange due to higher temperatures, enhanced by reduced fractionation during phytoplankton growth due to elevated CO_2 concentrations. Both processes lead to more negative δ^{13}C signatures in the surface ocean. Additionally, gross air-sea fluxes are increased as a result of the higher CO_2 concentrations, decreasing the air-sea disequilibrium. This leads to more negative δ^{13}C signatures in mid- and low-latitude surface waters and less negative in cold high-latitude waters (see e.g. Menviel et al., 2015). This surface to deep $\Delta\delta^{13}$C$_{DIC}$ gradient is dampened

20   in the case of experiment $p500$ by enhanced weathering of $CaCO_3$ on land, adding carbon with a positive δ^{13}C signature (∼2.9 ‰) to the surface ocean. As discussed above, these spatial $\Delta\delta^{13}$C gradients are important and co-govern the removal rate of the δ^{13}C perturbation. The larger than average δ^{13}C perturbation in the surface is communicated to phytoplankton and zooplankton, feeding the burial flux of biogenic material. This accelerates the removal of the δ^{13}C perturbation in comparison to a uniformly mixed ocean.

25   Next, the temporal evolution of the δ^{13}C$_{DIC}$ perturbation and its spatial pattern are described by PC-EOF (Fig. 4). The first PC-EOF pair captures approximately the δ^{13}C$_{DIC}$ evolution after 1 kyr, while the second and third PC-EOF pairs capture, toghether with the first pair, the decadal-to-century scale penetration of the perturbation into the ocean. The first EOF pattern (Fig. 4a) shows negative values throughout the ocean, with a pattern similar to that modelled for year 50,000 (Fig. 5g). The corresponding PC timeseries increases during the first decades after the pulse, followed by a slow decline on multi-millennial

30   timescales (Fig. 4b). This first PC captures the evolution of ocean mean $\Delta\delta^{13}$C$_{DIC}$ well after 1 kyr (Fig. 3 blue versus gray lines). In contrast to the first EOF, the second EOF has a clear dipole pattern with negative values in surface and intermediate waters and in the NADW region, and positive values below ∼ 1 km depth (Fig. 4c). The corresponding PC timeseries has high positive values in the first decades of the simulation, declining over the next centuries, becoming negative around year 500, and approaching zero on multi-millennial timescales. In combination with the first PC-EOF pair this leads to strongly negative
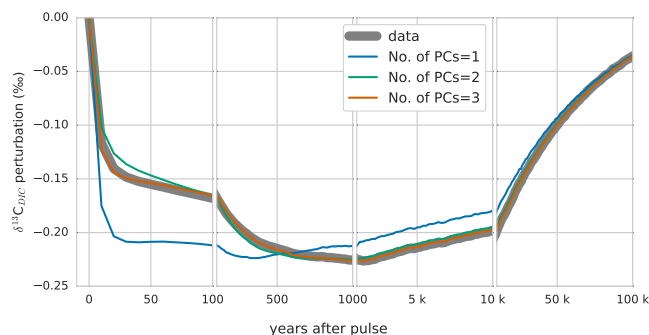
Figure 3. Modeled and reconstructed perturbation of δ^{13}C$_{DIC}$ with one, two, and three principal components for a 500 GtC carbon pulse with δ^{13}C = -24 ‰.
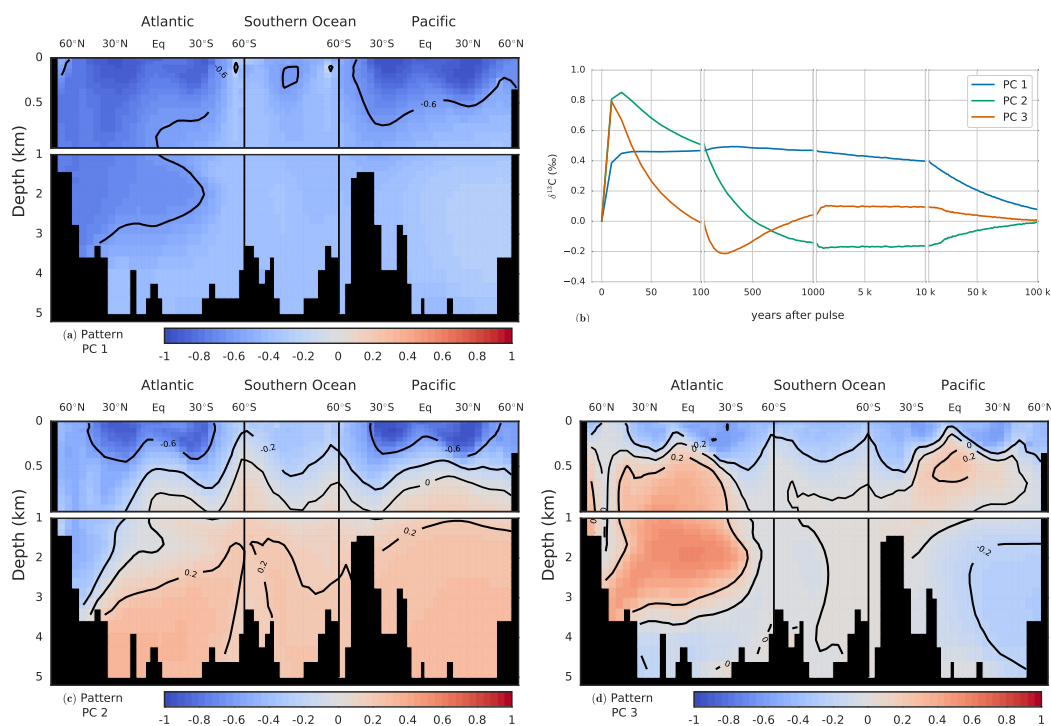

Figure 4. EOF pattern of the (a) first, (c) second, and (d) third principal component. Corresponding PC timeseries are shown in (b).

δ^{13}C values in surface and intermediate waters in the first centuries of the simulation whereas on longer timescales the depth gradient in $\Delta\delta^{13}$C$_{DIC}$ disappears. The third PC-EOF, finally, is of importance during the first century (Fig. 4b) and captures regional features, e.g. related to North Atlantic Deep Water or Intermediate Waters (Fig. 4d).

The global mean $\Delta\delta^{13}$C$_{DIC}$ is well described by the first two PCs (Fig. 3, green vs gray line). The third PC-EOF pair

5 mostly adds performance during the first century (cf. green and orange lines in Fig. 3) and reduces the root mean squared error

(RMSE) between reconstructed and modelled global mean $\Delta\delta^{13}\mathrm{C}_{DIC}$ from 0.003 ‰ with two PC-EOF pairs to 0.001 ‰ with three PC-EOF pairs used in the reconstruction.

   For the reconstruction of the spatio-temporal evolution of $\Delta\delta^{13}\mathrm{C}_{DIC}$, we will now use the first three PC-EOF pairs. The RMSE between the modelled and reconstructed 3-D field is highest (0.1 ‰) for the first 3-D output at year 10 after the pulse

5 and decreases to 0.03 ‰ at year 100. As visible from Fig. 5a and b, largest deviations between modeled and reconstructed $\Delta\delta^{13}\mathrm{C}_{DIC}$ are found in the thermocline of the Pacific and in the deep northern Atlantic. Further, the modelled perturbation has not yet propagated to the deep Pacific and Atlantic by year 100 (Fig. 5a), whereas the PC-EOF reconstruction displays a $\Delta\delta^{13}\mathrm{C}_{DIC}$ signal in these water masses. The performance of the reconstruction increases over the course of the simulation. The RMSE of the $\Delta\delta^{13}\mathrm{C}_{DIC}$ fields amounts to 0.01 ‰ at 1 and 10 kyrs and decreases to 0.007 ‰ 50 kyrs after the pulse.

10 Overall, reconstructing $\Delta\delta^{13}\mathrm{C}_{DIC}$ with three PC-EOF pairs shows good results and deviations from the modeled $\Delta\delta^{13}\mathrm{C}_{DIC}$ are of the order of 10 % of the perturbation and smaller on centennial to millennial timescales (Fig. 5d,f,h). To reconstruct the modelled evolution of $\Delta\delta^{13}\mathrm{C}_{DIC}$ precisely during the first few centuries after a perturbation, more than three PC-EOF pairs are necessary. In summary, the spatio-temporal evolution of $\Delta\delta^{13}\mathrm{C}_{DIC}$ over 100 years to 100 kyrs after a pulse input of carbon into the atmosphere is described accurately and conveniently by three PC-EOFs pairs.
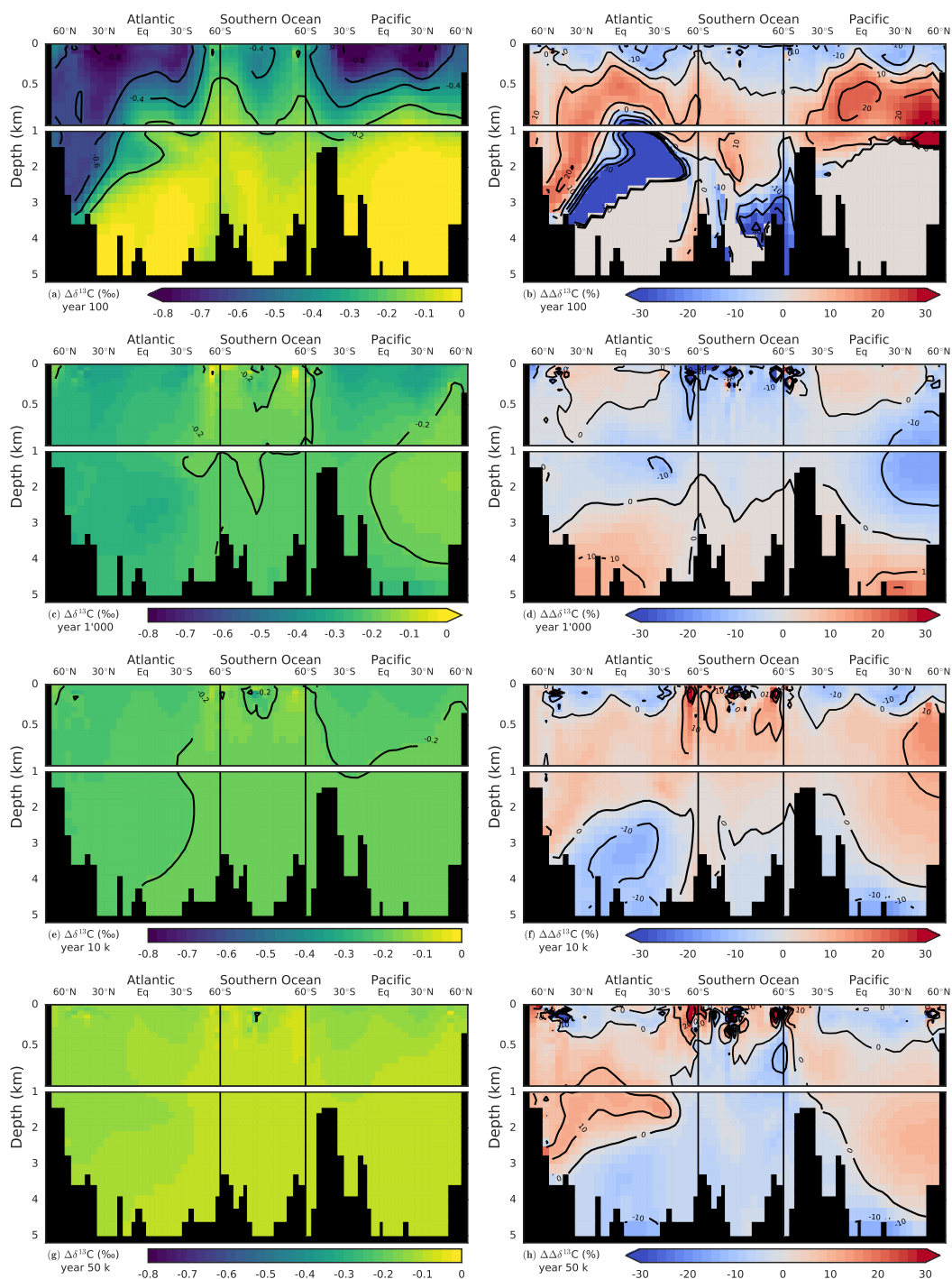
Figure 5. Modeled $\delta^{13}C_{DIC}$ perturbation (a,c,e,g) and difference between modeled and reconstructed $\delta^{13}C_{DIC}$ perturbation using the first three principal components in ‰ (b,d,f,h). Shown are time slices 100 years (a,b), 1 (c,d), 10 (e,f), and 50 (g,h) kyrs after the pulse release of carbon. Note that in panel (b) perturbation values smaller than |0.05| ‰ (abyssal Atlantic and Pacific) have been masked for better visibility as the perturbation has not yet propagated into these regions (see panel (a)).

Climate
of the Past
Discussions

3   Discussion and conclusion

The aim of this study is to investigate the evolution of a δ^{13}C perturbation in the Earth System in response to a carbon input to the atmosphere on time scales from centuries to 100 kyrs. To this end, the response of the Bern3D-LPX model was probed by pulse-like emissions of carbon to the atmosphere from an external source such as land biosphere carbon release or fossil fuel

5   burning. The δ^{13}C response is compared to that of atmospheric CO_2 and radiocarbon.

The impulse response (or Green's) functions (IRF) for atmospheric CO_2 and its δ^{13}C signature are fitted by a sum of exponential functions. Additionally, we show that the spatio-temporal evolution of a $\delta^{13}C_{DIC}$ perturbation is reasonably represented with three PC-EOF pairs. Deviations between the PC-EOF reconstruction and modeled $\delta^{13}C_{DIC}$ results are largest in the first decades after the pulse and are on the order of 10 % of the perturbation on millennial time scales. This allows the

10   construction of a computationally efficient substitute model which can be applied to investigate, e.g., reconstructed $\delta^{13}C_{DIC}$ variations from marine sediments in future studies. The evolution of the atmospheric CO_2 perturbation in the coupled Bern3D-LPX model is comparable to results from earlier studies addressing the pulse-like input of carbon into the atmosphere (e.g. Maier-Reimer and Hasselmann, 1987; Siegenthaler and Joos, 1992; Archer et al., 1998; Ridgwell and Hargreaves, 2007; Archer et al., 2009; Colbourn et al., 2015; Lord et al., 2015). The inclusion of peat lands in the LPX-Bern model adds a

15   (small) additional sink on multi-millennial timescales, previously not considered in such simulations. For the carbon isotopes, corresponding long-term pulse response simulations that consider ocean-sediment and weathering feedbacks appear missing in the literature. The "short-term" response from years to a couple of millennia is consistent with earlier results (Joos and Bruno, 1996).

We quantify the processes leading to the different removal timescales of atmospheric CO_2 and $\delta^{13}C_{atm}$ perturbations with

20   the help of factorial experiments. The role of different processes are further illustrated by analytical descriptions derived from a two box atmosphere-ocean and three box atmosphere-ocean-land model provided in the Appendix. The removal of an atmospheric perturbation in the isotopic ratio ^{13}C/^{12}C is, unlike for CO_2, not buffered by marine carbonate chemistry. The atmospheric δ^{13}C perturbation is partitioned among the ocean, land biosphere, and atmosphere roughly in proportion to their carbon inventory over about 2 kyrs. This leaves only a very small fraction airborne (1 to 3 % for pulses of a few hundred

25   GtC) after the signal is mixed within these three reservoirs. In contrast, a substantial fraction of carbon emissions and the CO_2 perturbation remains airborne for millennia. On time scales of a few millennia to 20 kyrs, the initial atmospheric CO_2 perturbation is lowered by carbonate compensation to a fraction of about 8 %. In contrast, this chemical buffering does hardly affect the atmospheric δ^{13}C perturbation. On even longer time scales, the CO_2 and the isotopic perturbation is removed by different, though related processes. For δ^{13}C, the continuous flux of biogenic calcium carbonate and organic carbon particles

30   carries the isotopic perturbation from the surface ocean to the lithosphere. For CO_2, the excess weathering of silicate rocks in response to the CO_2 and climate perturbation adds alkalinity to the ocean which leads to a complete removal of the atmospheric CO_2 perturbation.

Gradients in the $\delta^{13}C_{DIC}$ perturbation strongly influence the long-term removal timescale of the isotopic perturbation. In the pulse experiments, $\Delta\delta^{13}$C is enlarged in the surface ocean by temperature-dependent fractionation during air-sea gas exchange

(Mook, 1986), CO_2-dependent fractionation by phytoplankton (Freeman and Hayes, 1992), and altered air-sea disequilibrium resulting from changes in gross exchange fluxes due to altered CO_2. Changes in $CaCO_3$ weathering on the other hand, diminish the surface perturbation (e.g. experiment $p500$ vs SED_{500} in Fig. 1a). As a result, the isotopic perturbation is removed faster by particle burial than expected from a uniformly mixed ocean. This highlights the importance to resolve spatial structures in the perturbation to represent its removal time scales. More generally and beyond pulse release experiments, any process that changes the δ^{13}C signature of the relentless flux of organic and calcium carbonate particles, will influence the δ^{13}C loss flux from the ocean-atmosphere-land biosphere system to the litosphere (for examples see (Jeltsch-Thömmes et al., 2019; Roth et al., 2014; Tschumi et al., 2011)).

Our results have consequences for the interpretation of the difference in δ^{13}C between similar climate states such as the Penultimate Glacial Maximum (PGM) and the Last Glacial Maximum (LGM) or between the Eem and the Holocene warm periods. Substantial temporal δ^{13}C differences between these periods are recorded in ice cores (Schneider et al., 2013; Eggleston et al., 2016) and in marine sediments (Hoogakker et al., 2006; Oliver et al., 2010). Different mechanisms, such as changes in the δ^{13}C signature of weathering and burial fluxes, varying contribution of volcanic outgassing of CO_2, and changes in the amount of carbon stored in the land biosphere, especially in yedoma and permafrost soils, have been discussed for the PGM-LGM δ^{13}C offset (e.g. Lourantou et al., 2010; Schneider et al., 2013) An internal reorganization of the marine carbon cycle without considering changes in burial can not explain the offset as the δ^{13}C signature of the combined atmosphere-ocean system changed. However, internal marine carbon cycle reorganizations, e.g., due to changes in circulation, may have altered δ^{13}C in the surface ocean, and in turn δ^{13}C of the burial flux, and thereby the balance between weathering input and burial. The Bern3D results suggest that changes in organic carbon storage on land (or in the ocean) are not a likely explanation of the isotopic offset. Rather, long-term imbalances in the weathering, volcanic, and burial fluxes appear to be a plausible cause. Schneider et al. (2013) estimated required changes in land carbon storage to match the ice core and marine temporal offsets in δ^{13}C using preliminary Bern3D results for pulse release simulations. Our results show, in agreement with these earlier results, that the isotopic perturbation associated with a terrestrial carbon release is attenuated to less than 15 % within two millennia for pulse sizes of up to 5,000 GtC and declines thereafter (see black line in Fig. 1b). This would require several thousand GtC to have been stored additionally in the land biosphere during the LGM compared to the PGM in order to explain the δ^{13}C offset (see also Schneider et al., 2013). This amount seems large in light of estimated total carbon stocks of $\sim$1500 GtC in perennially frozen soils in Northern Hemisphere permafrost regions today (Tarnocai et al., 2009) and an even smaller inventory at the LGM Lindgren et al. (2018).

Further, the different behavior of CO_2 and $\delta^{13}C_{atm}$ perturbations has also consequences for centennial scale CO_2 and $\delta^{13}C_{atm}$ variations such as during Heinrich Stadial (HS) 4 and 1. Variations in CO_2 and $\delta^{13}C_{atm}$ during HS4 and HS1 have been measured on Antarctic ice cores and show an increase in CO_2 on the order of $\sim$10 ppm over 200-300 years. The increase in CO_2 is accompanied by a decrease in $\delta^{13}C_{atm}$ of $\sim$0.2 ‰ . These changes have been attributed to a release of terrestrial carbon to the atmosphere (Bauska et al., 2016, 2018). From our experiments and eqs. 5 and 6, however, we would expect for a centennial scale event a stronger increase in CO_2 for a decrease in $\delta^{13}C_{atm}$ of $\sim$0.2 ‰. Idealized simulations show that releases of varying amounts of terrestrial carbon with δ^{13}C = -24 ‰ over 100 to 400 years yield a linear response in ΔCO_2
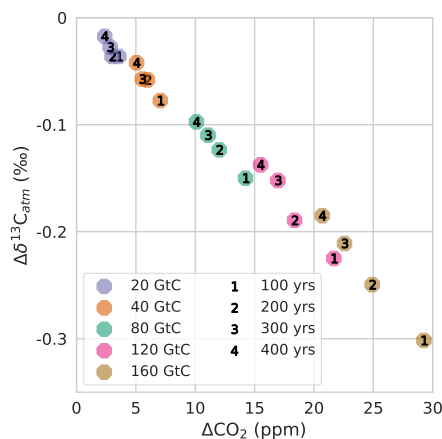
Figure 6. Response in ΔCO_2 and $\Delta\delta^{13}C_{atm}$ to a uniform release of 20, 40, 80, 120, and 160 GtC (colors) of isotopically light carbon ($\delta^{13}C$ = -24 ‰) to the atmosphere over 100, 200, 300, and 400 years (numbers). Shown is the mean over 30 years starting in the last year of the release.

and $\Delta\delta^{13}C_{atm}$ (Fig. 6). For a $\delta^{13}C_{atm}$ decrease of ∼0.2 ‰ the results indicate a CO_2 change of about 20 ppm rather than 10 ppm (Fig. 6). This estimate of 20 ppm may represent an upper limit as the assumed $\delta^{13}C$ signature of -24 ‰ is for C3 plants and negative compared to that of C4 plants, which were potentially favored during the glacial (Collatz et al., 1998). Also, the values shown in Fig. 6 are 30-year means. A wider gas age distribution would reduce the perturbation in $\delta^{13}C_{atm}$

5   more than in CO_2 (see e.g. Köhler et al., 2011). An external input, such as a release of terrestrial carbon to the atmosphere, as sole mechanism for the CO_2 and $\delta^{13}C_{atm}$ excursion during HS4 and HS1 seems thus unlikely.

In conclusion, the responses in atmospheric CO_2 and in $\delta^{13}C_{atm}$ to a carbon input (or removal) are different, with implications for the interpretation of paleo proxy data. The difference in response is related to the aquatic carbonate chemistry and the burial weathering cycle, which affect $CO_{2,a}$ and its isotopic ratio differently.

10   *Data availability.* Pulse response data and EOF patterns and PC timeseries will be made available for download on http://www.climate.unibe.ch/research/research_groups/earth_system_modelling_biogeochemical_cycles/index_eng.html

Further data upon request to the corresponding author.

Appendix A: Analytical expressions for the Impulse Response Functions of $CO_{2,a}$ and $\delta^{13}C_a$

Ocean invasion of an atmospheric CO_2 perturbation: The difference in the IRF for carbon and the isotopic ratios can be

15   understood in terms of the aquatic carbonate chemistry. We develop approximate expressions for the IRF of atmospheric CO_2 (eq. A7) and $\delta^{13}C$ (eq. A29), starting in this section with IRF(CO_2).

For small pulses, changes in sea surface temperature and in CO_2 solubility, changes in ocean circulation, and changes in the marine biological cycle are small and neglected in the following. Changes in land biosphere carbon storage can be considerable, in particular during the first century. However, the role of land carbon stock changes becomes smaller, the more carbon is taken up by the ocean and can be neglected again.

5   We consider a two box model of the atmosphere (index: a) and ocean (index: o) with area $A=A_a=A_o$ and heights h_a and h_o. Before the pulse addition, the model is in equilibrium and the initial CO_2 partial pressure is $pCO_{2,0}=pCO_{a,0}=pCO_{o,0}$. The initial concentration in the atmosphere is $C_{a,0}$. In the ocean, the initial dissolved inorganic carbon (DIC) concentration is DIC_0. The carbon inventories in the atmosphere and ocean are $N_a=C_a \cdot h_a \cdot A$ and $N_o=DIC \cdot h_o \cdot A$. We express the atmospheric partial pressure and inventory in units of DIC_0 and define an atmospheric concentration, C_a:

$$C_a = \frac{pCO_{2,a}}{pCO_{2,0}} DIC_0, \tag{A1}$$

and scale height h_a:

$$h_a = \frac{N_{a,0}}{A \cdot DIC_0}. \tag{A2}$$

The perturbation (Δ) from the initial equilibrium in pCO_2, and similarly for other quantities, is defined by: $\Delta pCO_2(t)=$ $pCO_2(t)-pCO_2(t_0)$. The perturbation in $pCO_{2,o}$ is related to that in DIC by the Revelle factor ξ (Revelle and Suess, 1957):

15

$$\xi = \frac{\Delta pCO_{2,o}}{pCO_{2,0}} \cdot \frac{DIC_0}{\Delta DIC} \tag{A3}$$

This yields for the perturbation in the net air-to-sea carbon flux per unit area, $\Delta f_{a->o,net}$:

$$\Delta f_{a->o,net} = k_g \cdot (\Delta pCO_{2,a} - \Delta pCO_{2,o}) = g \cdot (\Delta C_a - \xi \Delta DIC), \tag{A4}$$

$\Delta pCO_{2,a}$ and $\Delta pCO_{2,o}$ were replaced with the help of eq. A1 and A3 to obtain the right-hand side of eq. A4. k_g is the gas
20   transfer rate relative to the partial pressure (Wanninkhof, 1992) and g the rate relative to DIC:

$$g = k_g \cdot \frac{pCO_{2,0}}{DIC_0}. \tag{A5}$$

The IRF, or equivalent the airborne fraction, is defined by:

$$IRF(CO_{2,a}(t)) = \frac{\Delta N_a(t)}{P} = \frac{\Delta N_a(t)}{\Delta N_a(t) + \Delta N_o(t)}, \qquad \text{for } t > t_0 \tag{A6}$$

P is the magnitude of the initial carbon pulse at time t_0 and this released carbon is conserved within the model atmosphere
25   and ocean. The net air-to-sea flux becomes zero, when a new equilibrium at time t_∞ is reached; it follows from eq. A1 that $C_{a,0} =DIC_0$ and from eq. A4 that $\Delta DIC_\infty = \Delta C_{a,\infty}/\xi$. Finally, using this and $\Delta N_a = \Delta C_a \cdot h_a \cdot A$ and $\Delta N_o = \Delta DIC \cdot h_o \cdot A = \Delta C_a/\xi \cdot h_o \cdot A$ yields for the IRF in an ocean-atmosphere system at equilibrium:

$$IRF_\infty(CO_{2,a}) = \frac{h_a}{h_a + \frac{1}{\xi} h_o} = \frac{N_{a,0}}{N_{a,0} + \frac{1}{\xi} N_{o,0}}. \tag{A7}$$

Distribution of a δ^{13}C perturbation within the atmosphere-ocean-land biosphere system: We now turn to the isotope ^{13}C. The isotopic ratio is given by (see e.g. Mook, 1986)):

$$^{13}R(\text{C}) =^{13}\text{C}/^{12}\text{C}, \tag{A8}$$

and the isotopic signature in permil by:

$$5 \quad \delta^{13}\text{C} = \left(\frac{^{13}R}{^{13}R_{std}} - 1 \right) \cdot 1000. \tag{A9}$$

$^{13}R_{std}$ is the standard ratio. Isotopic discrimination is described by factors using the symbol α or by additive terms in δ-notation using symbol ε in permil. It holds:

$$\varepsilon = (\alpha - 1) \cdot 1000. \tag{A10}$$

In the following, we neglect for simplicity the order 1% difference between the concentration of ^{12}C and total C (this difference 10 may be accounted for in the definition and values of the isotopic discrimination factors).

We address first the response during the first two millennia after the pulse. In the following paragraphs, we will develop a simple analytical expression for the IRF (δ^{13}C$_a$) after a new equilibrium for the atmosphere-ocean-land biosphere system is reached. Thus, we neglect carbonate compensation and weathering and burial fluxes. We consider exchange between the atmosphere and ocean, and between the atmosphere and land biosphere reservoirs and assume that these three reservoirs are 15 well mixed.

The box model: The carbon and ^{13}C budgets for the 3-box model are described by:

$$\begin{aligned}
\frac{dN_o^i}{dt} &= F_{a->o}^i - F_{o->a}^i = F_{a->o,net}^i \\
\frac{dN_b^i}{dt} &= F_{a->b}^i - F_{b->a}^i = F_{a->b,net}^i \\
\frac{dN_a^i}{dt} &= -F_{a->o,net}^i - F_{a->b,net}^i + \delta(t) \cdot P^i
\end{aligned} \tag{A11}$$

20 N is the reservoir size (e.g. in GtC), indices a, o, and b denote the atmosphere, ocean, and land biosphere box, respectively. Index i refers either to carbon or ^{13}C. F denotes fluxes between reservoirs. δ is the Kronecker symbol and P^i the pulse released at time $t = t_0 = 0$ to the atmosphere.

The initial atmospheric δ^{13}C perturbation: The IRF(t) for δ^{13}C$_a$ is given by the perturbation in the isotopic signature, $\Delta\delta^{13}$C$_a$(t), divided by the initial (ini) perturbation. $\Delta\delta^{13}$C$_a^{ini}$. $\Delta\delta^{13}$C$_a^{ini}$ is the perturbation immediately after a carbon input 25 of amount P and with signature ^{13}R$_P$ (δ^{13}C$_P$). Mass balance implies that the amount of ^{13}C before and after the pulse release is equal:

$$N_{a,0} \cdot {}^{13}R_{a,0} + P \cdot {}^{13}R_P = (N_{a,0} + P) \cdot {}^{13}R_a^{ini}. \tag{A12}$$

We convert the ratios to δ-units and subtract on both sides $(N_{a,0} + P) \cdot \delta^{13}C_{a,0}$ to get the initial perturbation:

$$\Delta\delta^{13}\text{C}_a^{ini} = \frac{P}{N_{a,0} + P} \cdot (\delta^{13}\text{C}_P - \delta^{13}\text{C}_{a,0}). \tag{A13}$$

$\Delta\delta^{13}C_a^{ini}$ is proportional to the difference between the signature of the pulse and the initial atmospheric signature. Thus, the initial perturbation is relative to the atmospheric $\delta^{13}C$ signature.

The relationship between $\delta^{13}C_a$, $\delta^{13}C_o$, and $\delta^{13}C_b$ at equilibrium: In this subsection, relationships between the isotopic signatures are developed by considering equilibrium between the three boxes. This will allow us to simplify the isotopic mass balance equations further below .

The gross air-to-sea flux per unit area is:

$$^{13}f_{a->o} = {}^{13}k_g \cdot {}^{13}pCO_{2,a} = k_g \cdot pCO_{2,a} \cdot {}^{13}\alpha_{a->o} \cdot {}^{13}R(pCO_{2,a}), \tag{A14}$$

where $^{13}\alpha_{a->s}={}^{13}k_g/k_g$ is the discrimination factor for the gross air-to-sea transfer. The gross sea-to-air flux is:

$$
\begin{aligned}
^{13}f_{o->a} = {}^{13}k_g \cdot {}^{13}pCO_{2,o} &= k_g \cdot pCO_{2,o} \left(\frac{{}^{13}k_g}{k_g} \frac{{}^{13}R(pCO_{2,o})}{{}^{13}R(DIC)} \right) \cdot {}^{13}R(DIC) \\
&= k_g \cdot pCO_{2,o} \cdot {}^{13}\alpha_{o->a} \cdot {}^{13}R(DIC). \tag{A15}
\end{aligned}
$$

The term in parentheses is the the discrimination factor for the transfer of carbon from the DIC pool to the atmosphere, $^{13}\alpha_{o->a}$. At equilibrium (eq), the two gross fluxes cancel each other. It follows with $pCO_{2,a,eq} = pCO_{2,o,eq}$ and $^{13}pCO_{2,a,eq} = {}^{13}pCO_{2,o,eq}$:

$$^{13}R_{eq}(pCO_{2,a}) = \frac{{}^{13}\alpha_{o->a}}{{}^{13}\alpha_{a->o}} \cdot {}^{13}R_{eq}(DIC) = \frac{1}{\alpha_{a,o}} \cdot {}^{13}R_{eq}(DIC). \tag{A16}$$

This equation gives the equilibrium relationship between the atmospheric and oceanic signature. $\alpha_{a,o}$ denotes the equilibrium discrimination factor between $pCO_{2,a}$ and DIC. $\alpha_{a,o}$ depends on temperature and somewhat on carbonate chemistry (Mook, 1986) and is about 1.008 and thus close to 1.

A similar relationship is readily developed for the isotopic ratio of the total carbon in the land biosphere. The gross fluxes between the land and atmosphere are:

$$
\begin{aligned}
^{13}F_{a->b} &= F_{a->b} \cdot {}^{13}\alpha_{a->b} \cdot {}^{13}R(pCO_{2,a}) \\
^{13}F_{b->a} &= F_{b->a} \cdot {}^{13}\alpha_{b->a} \cdot {}^{13}R(N_b). \tag{A17}
\end{aligned}
$$

This yields at equilibrium:

$$^{13}R_{eq}(pCO_{2,a}) = \frac{1}{\alpha_{a,b}} \cdot {}^{13}R_{eq}(N_b) \tag{A18}$$

Eqs. A16 and A18 are readily converted into δ notation:

$$
\begin{aligned}
\delta^{13}C_{o,eq} &= \left(1 + \frac{\varepsilon_{a,o}}{1000} \right) \delta^{13}C_{a,eq} + \varepsilon_{a,o} \cong \delta^{13}C_{a,eq} + \varepsilon_{a,o}. \\
\delta^{13}C_{b,eq} &= \left(1 + \frac{\varepsilon_{a,b}}{1000} \right) \delta^{13}C_{a,eq} + \varepsilon_{a,b} \cong \delta^{13}C_{a,eq} + \varepsilon_{a,b}. \tag{A19}
\end{aligned}
$$

Eqs. A16, A18 and A19, allow us to express the isotopic signature of the land biosphere and the ocean by the isotopic signature of the atmosphere at equilibrium. These equations hold both for the initial equilibrium (t_0) before the pulse release

and when a new equilibrium is reached at t_∞. In practice is t_∞ about 2 kyrs. It follows immediately from eq. A19 that the isotopic signatures at the new equilibrium are about equal for the three reservoirs:

$$\Delta\delta^{13}C_\infty = \Delta\delta^{13}C_{a,\infty} \cong \Delta\delta^{13}C_{o,\infty} \cong \Delta\delta^{13}C_{b,\infty}. \tag{A20}$$

In other words, the isotopic signal is mixed uniformly through the atmosphere, ocean, and land biosphere when assuming that

5 these three reservoirs are well mixed as in this Appendix section.

Solving the mass balance equations of the isotopic pertubation for $\Delta\delta^{13}C$: The mass balance equations for the ocean-land biosphere-atmosphere system are given for carbon by:

$$
\begin{aligned}
N_{a,0} + N_{o,0} + N_{b,0} + P &= N_{a,\infty} + N_{o,\infty} + N_{b,\infty}, &&\text{for } t > t_0 \\
P &= \Delta N_a + \Delta N_o + \Delta N_b.
\end{aligned} \tag{A21}
$$

10 The second equation, describes the perturbation only. We use eqs. A16 and A18 to replace $N_o \cdot {}^{13}R_o$ with $\alpha_{a,o} \cdot N_o \cdot {}^{13}R_a$ and similar for the land reservoir and write the mass balance for ^{13}C:

$$
\begin{aligned}
&(N_{a,0} + \alpha_{a,o} \cdot N_{o,0} + \alpha_{a,b} \cdot N_{b,0}) \cdot {}^{13}R_{a,0} + P \cdot {}^{13}R_P &&\text{for } t > t_0 \\
&= (N_{a,\infty} + \alpha_{a,o} \cdot N_{o,\infty} + \alpha_{a,b} \cdot N_{b,\infty}) \cdot {}^{13}R_{a,\infty}.
\end{aligned} \tag{A22}
$$

Now we convert to δ units:

15
$$
\begin{aligned}
&(N_{a,0} + \alpha_{a,o} \cdot N_{o,0} + \alpha_{a,b} \cdot N_{b,0} + P) \cdot 1000 + (N_{a,0} + \alpha_{a,o} \cdot N_{o,0} + \alpha_{a,b} \cdot N_{b,0}) \cdot \delta^{13}C_{a,0} + P \cdot \delta^{13}C_P \\
&= (N_{a,\infty} + \alpha_{a,o} \cdot N_{o,\infty} + \alpha_{a,b} \cdot N_{b,\infty}) \cdot 1000 + (N_{a,\infty} + \alpha_{a,o} \cdot N_{o,\infty} + \alpha_{a,b} \cdot N_{b,\infty}) \cdot \delta^{13}C_{a,\infty}.
\end{aligned} \tag{A23}
$$

We subtract on both side the mass balance equation for carbon (eq. A21) multiplied by factor 1000. Note that $\alpha_{a,o}$ and $\alpha_{a,b}$ are present in the carbon terms in eq. A23, but not in the mass balance for carbon (eq. A21). This difference results in the first two terms in eq. A24 below.

20
$$
\begin{aligned}
&-\Delta N_{o,\infty} \cdot \overbrace{(\alpha_{a,o} - 1) \cdot 1000}^{\delta^{13}C_{DIC,0} - \delta^{13}C_{a,0}} \quad -\Delta N_{b,\infty} \cdot \overbrace{(\alpha_{a,b} - 1) \cdot 1000}^{\delta^{13}C_{b,0} - \delta^{13}C_{a,0}} \\
&+(N_{a,0} + \alpha_{a,o} \cdot N_{o,0} + \alpha_{a,b} \cdot N_{b,0}) \cdot \delta^{13}C_{a,0} + P \cdot \delta^{13}C_P \\
&= (N_{a,\infty} + \alpha_{a,o} \cdot N_{o,\infty} + \alpha_{a,b} \cdot N_{b,\infty}) \cdot \delta^{13}C_{a,\infty}.
\end{aligned} \tag{A24}
$$

Next, we subtract on both sides the third left hand side term, $(N_{a,0} + \alpha_{a,o} \cdot N_{o,0} + \alpha_{a,b} \cdot N_{b,0}) \cdot \delta^{13}C_{a,0}$, as well as the term $P \cdot \delta^{13}C_{a,0}$. We rearrange and use again the mass balance for carbon to get:

25
$$
\begin{aligned}
&-\Delta N_{o,\infty} \cdot (\delta^{13}C_{DIC,0} - \delta^{13}C_{a,0} \cdot (1 + \varepsilon_{a,o}/1000)) \\
&-\Delta N_{b,\infty} \cdot (\delta^{13}C_{b,0} - \delta^{13}C_{a,0} \cdot (1 + \varepsilon_{a,b}/1000)) - P \cdot (\delta^{13}C_a - \delta^{13}C_P) \\
&= (N_{a,0} + N_{o,0} \cdot (1 + \varepsilon_{a,o}/1000) + N_{b,0} \cdot (1 + \varepsilon_{a,b}/1000) + P) \cdot \Delta\delta^{13}C_{a,\infty}
\end{aligned} \tag{A25}
$$

Climate
of the Past
Discussions

Open Access

EGU

The terms with $\varepsilon/1000$ represent a small correction (< 0.02) and can be safely neglected. We replace P with $\Delta N_{a,\infty} + \Delta N_{o,\infty} + \Delta N_{b,\infty}$ in the above equation and exchange the left and right side to get the following mass balance for the δ^{13}C perturbation:

$$
\begin{aligned}
& (N_{a,0} + N_{o,0} + N_{b,0} + P) \cdot \Delta\delta^{13}\mathrm{C}_{a,\infty} \\
= & \ \Delta N_{a,\infty} \cdot \left(\delta^{13}\mathrm{C}_P - \delta^{13}\mathrm{C}_{a,0}\right) + \Delta N_{o,\infty} \cdot \left(\delta^{13}\mathrm{C}_P - \delta^{13}\mathrm{C}_{DIC,0}\right) + \Delta N_{b,\infty} \cdot \left(\delta^{13}\mathrm{C}_P - \delta^{13}\mathrm{C}_{b,0}\right) \\
= & \ P \cdot \left(\delta^{13}\mathrm{C}_P - \delta^{13}\mathrm{C}_{mean}\right),
\end{aligned}
\tag{A26}
$$

with:

$$
\delta^{13}\mathrm{C}_{mean} = \frac{\Delta N_{a,\infty}}{P} \cdot \delta^{13}\mathrm{C}_{a,0} + \frac{\Delta N_{o,\infty}}{P} \cdot \delta^{13}\mathrm{C}_{o,0} + \frac{\Delta N_{b,\infty}}{P} \cdot \delta^{13}\mathrm{C}_{b,0}
\tag{A27}
$$

Equation A26 represents the mass balance for the isotopic perturbation and its interpretation is as follows. The term on the left hand side equals the carbon mass in the system times the perturbation in the signature and therefore equals the total isotopic perturbation in GtC ‰ . In equilibrium, the δ^{13}C perturbation, $\Delta\delta^{13}\mathrm{C}_\infty$, is well mixed (eq. A20) within the total ocean-atmosphere carbon reservoir $(N_{a,0} + N_{o,0} + N_{b,0} + P)$. The terms after the first equal sign provide a different view of the total isotopic perturbation. In this picture, a fraction $\Delta N_{l,\infty}$ of the pulse is added to each reservoir (index l) with the perturbation in signature given by $(\delta^{13}\mathrm{C}_P - \delta^{13}\mathrm{C}_l)$. This is then summarized after the second equal sign by the product of the carbon input P times the isotopic perturbation of the pulse relative to the mean signature of the reservoirs absorbing this additional carbon, $\delta^{13}\mathrm{C}_P - \delta^{13}\mathrm{C}_{mean}$.

By rearranging eq. A26 we get the perturbation in the isotopic signature of the atmosphere-ocean-land system:

$$
\Delta\delta^{13}\mathrm{C}_\infty = \frac{P}{N_{a,0} + N_{o,0} + N_{b,0} + P} \cdot \left(\delta^{13}\mathrm{C}_P - \delta^{13}\mathrm{C}_{mean}\right).
\tag{A28}
$$

In other words, the perturbation in the signature scales with the carbon mass ratio of the pulse input to the total mass in the system. This perturbation is also proportional to the difference between the signature of the pulse and the "mean" signature of the system as defined by eq. A27.

IRF($\delta^{13}C_a$) at equilibrium (t ∼ 2 kyrs): Finally, we use the definition for the IRF and eqs. A13 and A28 to obtain the following expression for the IRF at a new equilibrium for the ocean-atmosphere-land biosphere system:

$$
\begin{aligned}
\mathrm{IRF}_\infty(\delta^{13}\mathrm{C}_a) & = \frac{\Delta\delta^{13}\mathrm{C}_{a,\infty}}{\Delta\delta^{13}\mathrm{C}_a^{ini}} \\
& = \frac{N_{a,0} + P}{N_{a,0} + N_{o,0} + N_{b,0} + P} \cdot \frac{(\delta^{13}\mathrm{C}_P - \delta^{13}\mathrm{C}_{mean})}{(\delta^{13}\mathrm{C}_P - \delta^{13}\mathrm{C}_{a,0})}
\end{aligned}
\tag{A29}
$$

The fraction of the initial perturbation in the atmosphere that remains airborne corresponds roughly to the ratio of the carbon in the atmosphere immediately after the pulse release to the total carbon in the system. The second fraction on the right side modifies this ratio by about +20 % for typical negative isotopic pulse perturbation applied in this study, because the mean signature is slightly heavier than the atmospheric signature. The nominator of this modifier reflects that the pulse perturbation is distributed within the system at the new equilibrium, while the denominator reflects that the pulse is initially added to the atmosphere.

Ocean invasion: numerical examples: Equation A7 and eq. A29 provide simple expressions to approximate the IRF for the perturbation in atmospheric CO_2 and its istopic signature after a pulse-like carbon input. These equations illustrate the fundamental difference in the IRF for $CO_{2,a}$ and for $\delta^{13}C_a$. To ease interpretation, we neglect the land biosphere for the moment. Then, in the limit of $P- > 0$, eq. A7 and eq. A29 are formally identical for carbon and ^{13}C (index: i):

$$IRF^i \overset{P \to 0}{\cong} \frac{N_{a,0}}{N_{a,0} + \frac{1}{\xi^i} N_{o,0}} \cdot M^i \tag{A30}$$

However, for $\delta^{13}C_a$ a Revelle Factor of 1 instead of about 12 applies, while the modifier M is exactly 1 for $CO_{2,a}$ and around 1 for $\delta^{13}C_a$. The perturbation in the isotopic signature is diluted by the entire carbon inventory in the system, whereas the "available" ocean inventory is reduced by the Revelle Factor for the dilution of an atmospheric CO_2 pertubation.

Numerically, the preindustrial carbon inventory is $600\,GtC$ in the atmosphere and $37,400\,GtC$ in the ocean. These values are equivalent to a scale height of 69 m for the atmosphere and of 4,300 m for the ocean, when assuming a preindustrial (surface) concentration of DIC of 24 g/m^3 and an ocean area of $3.62 \cdot 10^{14}$ m^2. The buffer factor is about 12 for small perturbations. This yields for $IRF_\infty(CO_{2,a})$ a value of about 0.16. In other words, a fraction of about 16 % of a (small) carbon input into the atmosphere is still airborne after about 1 to 2 kyrs, when the ocean and atmosphere have approached a new equilibrium. The observed penetration of CFCs and bomb-produced radiocarbon suggests that an atmospheric perturbation penetrates about the top 300 m of the ocean within a decade. Thus, we expect that about 70 % of the initial perturbation are still found in the atmosphere after a decade. These numbers are comparable in magnitude to the IRF of CO_2 shown in Fig. 1a for 10 years and 2 kyrs after the pulse input. The buffer factor increases with the magnitude of the perturbation in DIC and pCO$_2$ and thus with pulse size P. Hence, IRF increases with increasing pulse size, as again shown in Fig. 1a. We note that any carbon uptake or release by the land biosphere is not taken into account in eq. A7 and in this discussion, in contrast to the results discussed in the main text.

To determine the IRF for $\delta^{13}C_a$, we take into account that the isotopic signal is also entering the land biosphere and assume a total inventory in the atmosphere-ocean–land system of 40,000 GtC. This yields an IRF_∞ of 1 % to 3.2 % for P varying between -250 to +500 GtC and of about 18 % for P equal 5,000 GtC and using $\delta^{13}C_{mean}$=4 ‰ (calculated with eq. A27). These values are in agreement with the estimates shown in Fig. 1b for year 2,000. Assuming that the isotopic perturbation has mixed within a layer of 300 m in the ocean (2,600 GtC) and with the living vegetation on land (500 GtC) yiels a "decadal" IRF of about 12-31 % for small pulse sizes (-250 GtC to 500 GtC), again in agreement with the Bern3D-LPX results.

Carbonate compensation and terrestrial neutralization of the CO_2 perturbation: Next, we address CaCO$_3$ compensation of the carbon added by the pulse. We derive an expression for the IRF($CO_{2,a}$) at the time when CaCO$_3$ compensation of the pulse is completed - about 10-20 kyrs after the pulse input. The following calculations are based on Archer et al. (1998). As above, we assume the ocean to consist of a single, well-mixed box which is, after CaCO$_3$ compensation, again in equilibrium with the atmosphere. Concentrations of CO_2, HCO_3^-, and CO_3^{2-} in seawater are related by

$$\frac{pCO_{2,o} \cdot [CO_3^{2-}]}{[HCO_3^-]} = \frac{K_2' \cdot K_H}{K_1'} = const. \tag{A31}$$

$K_1^{'}$ and $K_2^{'}$ are the apparent dissociation constants for carbonic acid and K_H is the Henry's Law solubility product for CO_2. For simplicity, we assume the ratio of $K_1^{'}$, $K_2^{'}$, and K_H, which are temperature and salinity dependent, to be constant over the course of the experiments. With above assumption and by taking the ratio of initial and final states and by rearranging we get

$$\frac{pCO_{2,\infty}}{pCO_{2,0}} \approx \left(\frac{[HCO_{3,\infty}^-]}{[HCO_{3,0}^-]} \right)^2 \cdot \frac{[CO_{3,0}^{2-}]}{[CO_{3,\infty}^{2-}]}. \tag{A32}$$

5   Sedimentary dissolution of $CaCO_3$ in response to the carbon pulse tends to keep the carbonate ion concentration constant over the course of the simulations, yielding

$$\frac{pCO_{2,\infty}}{pCO_{2,0}} \approx \left(\frac{[HCO_{3,\infty}^-]}{[HCO_{3,0}^-]} \right)^2. \tag{A33}$$

HCO_3^- is by far the dominant form of DIC. This allows one to approximate HCO_3^- by DIC in eq. A33 to get:

$$\frac{pCO_{2,\infty}}{pCO_{2,0}} \approx \left(\frac{DIC_{o,0} + \Delta DIC_o}{DIC_{o,0}} \right)^2 = \left(\frac{N_{o,0} + \Delta N_o}{N_{o,0}} \right)^2. \tag{A34}$$

10   Δ refers here to the difference between the final and initial state. With pulse sizes substantially smaller than the oceanic DIC inventory, $\Delta N_o \ll N_{o,0}$ we approximate

$$\frac{pCO_{2,\infty}}{pCO_{2,0}} \approx 1 + 2 \cdot \frac{\Delta N_o}{N_{o,0}}. \tag{A35}$$

From Fig. 2b we see that on multi-millennial timescales the majority of the pulse is taken up by the ocean. Further, $CaCO_3$ compensation and weathering-burial imbalances in the $CaCO_3$ cycle (terrestrial neutralization) add (or remove) additional

15   carbon to (from) the ocean. We thus assume $\Delta N_o \approx 1.5 \cdot P$; P is the pulse size in GtC. The factor 1.5 is model dependent and slightly different here from the value provided by Archer et al. (1998) or in previous versions of the Bern3D model. This yields for the relative increase in pCO_2:

$$\frac{\Delta pCO_2}{pCO_{2,0}} \approx 3 \cdot \frac{P}{N_{o,0}}. \tag{A36}$$

We recall the definition of the airborne fraction:

20   $$IRF(CO_{2,a}) = 2.12 \ GtC \ \mu \ atm^{-1} \cdot \frac{\Delta pCO_{2,a}}{P}. \tag{A37}$$

Finally, with eq. A36 and A37 we express the IRF at the time when $CaCO_3$ compensation is completed by

$$IRF_{CaCO_3}(CO_{2,a}) = 3 \cdot 2.12 \ GtC \ \mu atm^{-1} \cdot \frac{pCO_{2,0}}{N_{o,0}}. \tag{A38}$$

The remaining atmospheric fraction is thus independent of the pulse size for $P \ll N_{o,0}$. Its magnitude results directly from the carbonate chemistry (Archer et al., 1998). With a pre-industrial ocean DIC inventory of 37,400 GtC and surface ocean pCO_2

25   of 284 μatm we get a remaining airborne perturbation of $\sim 5 \ \%$. This is in agreement with results from the Bern3D-LPX model after about 10-20 $kyrs$ (Fig. 1a).

Carbonate compensation of the δ^{13}C perturbation: Carbonate compensation has almost a negligible influence on the δ^{13}C perturbation. The carbonate compensation process acts, aside from small isotopic discrimination, equally on the different isotopes. Therefore, ^{12}CO$_{2,a}$ and ^{13}CO$_{2,a}$ both decrease according to eq. A38, leaving the isotopic ratio in first order approximation unchanged. Additional effects are, here formulated for a positive pulse, as follows. The dissolution of CaCO$_3$ adds

5   an isotopic perturbation to the ocean-atmosphere-land system. The amount of carbon added corresponds to about half of the pulse size, P. CaCO$_3$ has a δ^{13}C signature of about +2.9 ‰ compared to -24 ‰ of the pulse. We reference the CaCO$_3$ isotopic perturbation relative to the mean signature of the ocean in the model ($\sim$0.8 ‰) as this additional carbon remains mainly in the ocean, while the mean signature that applies for the pulse is according to eq. A27 about -3 ‰ for pulse sizes between -250 GtC and 500 GtC. Thus the isotopic perturbation by CaCO$_3$ dissolution is about 20 times smaller than that of the pulse

10   ($0.5 \times P \times$ (2.9 ‰ - 0.8 ‰) : $P \times (-24$ ‰ + 3 ‰) = -1:20). The dissolution of CaCO$_3$ enlarges the carbon reservoir by which the initial atmospheric δ^{13}C is diluted. However, the amount of added carbon is, except for the 5,000 GtC pulse, small compared the total inventory of the system of about 40,000 GtC. In summary, the influence of CaCO$_3$ compensation on δ^{13}C$_a$ is small and eq. A29 is still approximately valid for the time scale of CaCO$_3$ compensation.

Removal of the remaining CO$_2$ perturbation by silicate weathering: Finally, on timescales of hundreds of thousands

15   of years imbalances in the weathering and burial fluxes remove any remaining perturbation in carbon from the atmosphere-ocean-land system. Silicate rock weathering leads to a net removal of carbon from the atmosphere by the following simplified reaction (see Colbourn et al., 2013, for more details):

$$2CO_{2(aq)} + H_2O_{(l)} + CaSiO_{3,(s)} \rightarrow Ca^{2+}_{(aq)} + 2HCO^-_{3(aq)} + SiO_{2(aq)}. \tag{A39}$$
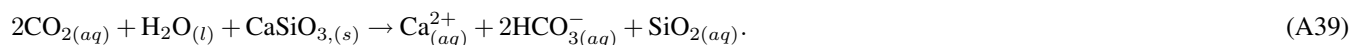
The timescale for this silicate weathering feedback has been determined to be on the order of 240 kyrs (Colbourn et al., 2015)

20   and 270 kyrs (Lord et al., 2015), however with a large spread. Silicate rock weathering removes the remaining atmospheric perturbation ($\sim$8 %). Further, the additional alkalinity added to the ocean deepens the saturation horizon, resulting in higher carbon burial in marine sediments and thus also removes the DIC perturbation (see Fig. 2a).

Removal of the remaining δ^{13}C perturbation by burial of organic matter and CaCO$_3$: In the case of δ^{13}C, silicate rock weathering has no direct effect on the δ^{13}C signature. The perturbation is removed on these long timescales by the replacement

25   of carbon through burial of organic matter and CaCO$_3$ and weathering inputs:

$$\frac{d}{dt}(N_S \cdot \Delta\delta^{13}C_S) = -F_{\text{burial}} \cdot \Delta\delta^{13}C_{burial}, \tag{A40}$$

with N_S and $\Delta\delta^{13}$C$_S$ equal the total mass and mean isotopic perturbation in the atmosphere-ocean-land system and F_{burial} the burial flux of carbon leaving the system and $\Delta\delta^{13}$C$_{burial}$ its isotopic signature. In simulations with constant weathering rates, the residence time of carbon in the atmosphere-ocean-land system is on the order of $\tau = N/F_{burial} \sim 90$ kyrs

30   (burial/weathering input is 0.46 GtC yr^{-1}, total amount: $\sim$ 40,000 GtC)). Surprisingly, in the factorial simulation with sediments and constant weathering fluxes (SED_{500}), the perturbation is removed much faster than expected from the mean residence time (Fig. 1b, dotted line), because the isotopic perturbation of the burial flux is larger than that of the ocean-atmosphere-land system.

The long-term removal rate of the δ^{13}C perturbation is sensitive to $\Delta\delta^{13}$C gradients in the ocean. The isotopic signature of the burial flux is mainly determined by the upper ocean signature. Changes in the gross exchange fluxes of carbon between the atmosphere and the ocean in response to perturbed CO_2 and changes in the isotopic fractionation of air-sea fluxes in response to perturbed temperatures increase the $\Delta\delta^{13}$C perturbation in the upper ocean relative to the deep. In case of enabled weathering

5 feedbacks, the additional flux of isotopically heavy carbon from excess weathering partly mitigates surface-to-deep $\Delta\delta^{13}$C gradients. In turn, the perturbation is removed faster in simulations with enabled weathering feedback compared to simulations with constant weathering. Taken together, this highlights the role of spatial patterns of the δ^{13}C perturbation even on these very long timescales.

Competing interests. The authors declare that they have no conflict of interest.

References

Archer, D. and Brovkin, V.: The millennial atmospheric lifetime of anthropogenic CO2, Climatic Change, 90, 283–297, https://doi.org/10.1007/s10584-008-9413-1, 2008.

Archer, D., Kheshgi, H., and Maier-reimer, E.: Multiple timescales for neutralization of fossil fuel CO2, Geophysical Research Letters, 24, 405–408, 1997.

Archer, D., Khesgi, H., and Maier-Reimer, E.: Dynamics of fossil fuel CO2 neutralization by marine CaCO3, Global Biogeochemical Cycles, 12, 259–276, 1998.

Archer, D., Eby, M., Brovkin, V., Ridgwell, A., Cao, L., Mikolajewicz, U., Caldeira, K., Matsumoto, K., Munhoven, G., Montenegro, A., and Tokos, K.: Atmospheric Lifetime of Fossil Fuel Carbon Dioxide, Annual Review of Earth and Planetary Sciences, 37, 117–134, https://doi.org/10.1146/annurev.earth.031208.100206, 2009.

Battaglia, G. and Joos, F.: Marine N2O Emissions From Nitrification and Denitrification Constrained by Modern Observations and Projected in Multimillennial Global Warming Simulations, Global Biogeochemical Cycles, 32, 92–121, https://doi.org/10.1002/2017GB005671, 2018a.

Battaglia, G. and Joos, F.: Hazards of decreasing marine oxygen: the near-term and millennial-scale benefits of meeting the Paris climate targets, Earth System Dynamics, 9, 797–816, https://doi.org/10.5194/esd-2017-90, https://www.earth-syst-dynam-discuss.net/esd-2017-90/, 2018b.

Battaglia, G., Steinacher, M., and Joos, F.: A probabilistic assessment of calcium carbonate export and dissolution in the modern ocean, Biogeosciences, 13, 2823–2848, https://doi.org/10.5194/bg-13-2823-2016, 2016.

Bauska, T. K., Baggenstos, D., Brook, E. J., Mix, A. C., Marcott, S. A., Petrenko, V. V., Schaefer, H., Severinghaus, J. P., and Lee, J. E.: Carbon isotopes characterize rapid changes in atmospheric carbon dioxide during the last deglaciation, Proceedings of the National Academy of Sciences, 113, 3465–3470, https://doi.org/10.1073/pnas.1513868113, 2016.

Bauska, T. K., Brook, E. J., Marcott, S. A., Baggenstos, D., Shackleton, S., Severinghaus, J. P., and Petrenko, V. V.: Controls on Millennial-Scale Atmospheric CO2 Variability During the Last Glacial Period, Geophysical Research Letters, 45, 7731–7740, https://doi.org/10.1029/2018GL077881, 2018.

Bereiter, B., Eggleston, S., Schmitt, J., Nehrbass-Ahles, C., Stocker, T. F., Fischer, H., Kipfstuhl, S., and Chappellaz, J.: Revision of the EPICA Dome C CO2 record from 800 to 600 kyr before present, Geophysical Research Letters, 42, 542–549, https://doi.org/10.1002/2014GL061957, 2015.

Brovkin, V., Ganopolski, A., Archer, D., and Munhoven, G.: Glacial CO2 cycle as a succession of key physical and biogeochemical processes, Climate of the Past, 8, 251–264, https://doi.org/10.5194/cp-8-251-2012, 2012.

Colbourn, G., Ridgwell, A., and Lenton, T. M.: The Rock Geochemical Model (RokGeM) v0.9, Geoscientific Model Development, 6, 1543–1573, https://doi.org/10.5194/gmd-6-1543-2013, 2013.

Colbourn, G., Ridgwell, A., and Lenton, T. M.: The time scale of the silicate weathering negative feedback on atmospheric CO2, Global Biogeochemical Cycles, 29, 583–596, https://doi.org/10.1002/2014GB005054, 2015.

Collatz, G. J., Berry, J. A., and Clark, J. S.: Effects of climate and atmospheric CO2 partial pressure on the global distribution of C 4 grasses: present, past, and future, Oecologia, 114, 441–454, https://doi.org/10.1007/s004420050468, http://link.springer.com/10.1007/s004420050468, 1998.

Dawson, A.: eofs: A Library for EOF Analysis of Meteorological, Oceanographic, and Climate Data, Journal of Open Research Software, 4, 4–7, https://doi.org/10.5334/jors.122, http://openresearchsoftware.metajnl.com/articles/10.5334/jors.122/, 2016.

Dickson, A. G., Sabine, C. L., and Christian, J. R., eds.: Guide to Best Practices for Ocean CO2 Measurements, PICES Special Publication 3, 2007.

5   Edwards, N. R., Willmott, A. J., and Killworth, P. D.: On the Role of Topography and Wind Stress on the Stability of the Thermohaline Circulation, Journal of Physical Oceanography, 28, 756–778, https://doi.org/10.1175/1520-0485(1998)028<0756:OTROTA>2.0.CO;2, 1998.

Eggleston, S., Schmitt, J., Bereiter, B., Schneider, R., and Fischer, H.: Evolution of the stable carbon isotope composition of atmospheric CO2 over the last glacial cycle, Paleoceanography, pp. n/a–n/a, https://doi.org/10.1002/2015PA002874, http://doi.wiley.com/10.1002/2015PA002874, 2016.

10   Enting, I. G., Wigley, T. M. L., and Heimann, M.: Future Emissions and Concentrations of Carbon Dioxide : Key Ocean / Atmosphere / Land Analyses, CSIRO, Division of Atmospheric Research Technical Paper, 31, 1–133, 1994.

Farquhar, G. D., von Caemmerer, S., and Berry, J. A.: A biochemical model of photosynthetic CO2 assimilation in leaves of C3 species, Planta, 149, 78–90, https://doi.org/10.1007/BF00386231, https://link.springer.com/content/pdf/10.1007/BF00386231.pdfhttp://link.springer.com/10.1007/BF00386231, 1980.

15   Freeman, H. and Hayes, J. M.: Fractionation of Carbon Isotopes by Phytoplankton and Estimates of Ancient CO2 Levels, Global Biogeochemical Cycles, 6, 185–198, 1992.

Ganopolski, A. and Brovkin, V.: Simulation of climate, ice sheets and CO2 evolution during the last four glacial cycles with an Earth system model of intermediate complexity, Climate of the Past, 13, 1695–1716, https://doi.org/10.5194/cp-13-1695-2017, 2017.

Griffies, S. M.: The Gent-McWilliams Skew Flux, Journal of Physical Oceanography, 28, 831–841, https://doi.org/10.1175/1520-0485(1998)028<0831:TGMSF>2.0.CO;2, 1998.

Harris, I., Jones, P. D., Osborn, T. J., and Lister, D. H.: Updated high-resolution grids of monthly climatic observations - the CRU TS3.10 Dataset, International Journal of Climatology, 34, 623–642, https://doi.org/10.1002/joc.3711, 2014.

Haxeltine, A. and Prentice, I. C.: BIOME3: An equilibrium terrestrial biosphere model based on ecophysiological constraints, resource availability, and competition among plant functional types, Global Biogeochemical Cycles, 10, 693–709, https://doi.org/10.1029/96GB02344, http://doi.wiley.com/10.1029/96GB02344, 1996a.

Haxeltine, A. and Prentice, I. C.: A General Model for the Light-Use Efficiency of Primary Production, Functional Ecology, 10, 551, https://doi.org/10.2307/2390165, https://www.jstor.org/stable/2390165?origin=crossref, 1996b.

Heinze, C., Maier-Reimer, E., Winguth, A. M. E., and Archer, D.: A global oceanic sediment model for long-term climate studies, Global Biogeochemical Cycles, 13, 221–250, 1999.

30   Hoogakker, B. A., Rohling, E. J., Palmer, M. R., Tyrrell, T., and Rothwell, R. G.: Underlying causes for long-term global ocean $\delta 13C$ fluctuations over the last 1.20 Myr, Earth and Planetary Science Letters, 248, 15–29, https://doi.org/10.1016/j.epsl.2006.05.007, 2006.

Hooss, G., Voss, R., Hasselmann, K., Maier-Reimer, E., and Joos, F.: A nonlinear impulse response model of the coupled carbon cycle-climate system (NICCS), Climate Dynamics, 18, 189–202, https://doi.org/10.1007/s003820100170, 2001.

Jeltsch-Thömmes, A., Battaglia, G., Cartapanis, O., Jaccard, S. L., and Joos, F.: Low terrestrial carbon storage at the Last Glacial Maximum: constraints from multi-proxy data, Climate of the Past, 15, 849–879, https://doi.org/10.5194/cp-15-849-2019, https://www.clim-past.net/15/849/2019/, 2019.

Joos, F. and Bruno, M.: Pulse response functions are cost-efficient tools to model the link between carbon emissions, atmospheric CO2 and global warming, Physics and Chemistry of The Earth, 21, 471–476, https://doi.org/10.1016/S0079-1946(97)81144-5, 1996.

Joos, F., Bruno, M., Fink, R., Siegenthaler, U., Stocker, T. F., and LeQuere, C.: An efficient and accurate representation of complex oceanic and biospheric models of anthropogenic carbon uptake, Tellus B: Chemical and Physical Meteorology, 48, 397–417, https://doi.org/10.1034/j.1600-0889.1996.t01-2-00006.x, 1996.

Joos, F., Prentice, I. C., Sitch, S., Meyer, R., Hooss, G., Plattner, G.-k., Gerber, S., and Hasselmann, K.: Global warming feedbacks on
5   terrestrial carbon uptake under the Intergovernmental Panel on Climate Change (IPCC) emission scenarios, Global Biogeochemical Cycles, 15, 891–907, 2001.

Joos, F., Roth, R., Fuglestvedt, J. S., Peters, G. P., Enting, I. G., Von Bloh, W., Brovkin, V., Burke, E. J., Eby, M., Edwards, N. R., Friedrich, T., Frölicher, T. L., Halloran, P. R., Holden, P. B., Jones, C., Kleinen, T., Mackenzie, F. T., Matsumoto, K., Meinshausen, M., Plattner, G. K., Reisinger, A., Segschneider, J., Shaffer, G., Steinacher, M., Strassmann, K., Tanaka, K., Timmermann, A., and Weaver, A. J.: Carbon
10   dioxide and climate impulse response functions for the computation of greenhouse gas metrics: A multi-model analysis, Atmospheric Chemistry and Physics, 13, 2793–2825, https://doi.org/10.5194/acp-13-2793-2013, 2013.

Kalnay, E., Kanamitsu, M., Kistler, R., Collins, W., Deaven, D., Gandin, L., Iredell, M., Saha, S., White, G., Woollen, J., Zhu, Y., Chelliah, M., Ebisuzaki, W., Higgins, W., Janowiak, J., Mo, K. C., Ropelewski, C., Wang, J., Leetmaa, A., Reynolds, R., Jenne, R., and Joseph, D.: The NCEP/NCAR 40-year reanalysis project, https://doi.org/10.1175/1520-0477(1996)077<0437:TNYRP>2.0.CO;2, 1996.

15   Keller, K. M., Lienert, S., Bozbiyik, A., Stocker, T. F., Churakova Sidorova, O. V., Frank, D. C., Klesse, S., Koven, C. D., Leuenberger, M., Riley, W. J., Saurer, M., Siegwolf, R., Weigt, R. B., and Joos, F.: 20th century changes in carbon isotopes and water-use efficiency: Tree-ring-based evaluation of the CLM4.5 and LPX-Bern models, Biogeosciences, 14, 2641–2673, https://doi.org/10.5194/bg-14-2641-2017, 2017.

Köhler, P., Fischer, H., and Schmitt, J.: Atmospheric d13CO2 and its relation to pCO2 and deep ocean d13C during the late Pleistocene,
20   Paleoceanography, 25, 1–16, https://doi.org/10.1029/2008PA001703, 2010.

Köhler, P., Knorr, G., Buiron, D., Lourantou, A., and Chappellaz, J.: Abrupt rise in atmospheric CO_2 at the onset of the Bølling/Allerød: in-situ ice core data versus true atmospheric signals, Climate of the Past, 7, 473–486, https://doi.org/10.5194/cp-7-473-2011, http://www.clim-past.net/7/473/2011/, 2011.

Krakauer, N. Y., Randerson, J. T., Primeau, F. W., Gruber, N., and Menemenlis, D.: Carbon isotope evidence for the latitudinal distribution
25   and wind speed dependence of the air-sea gas transfer velocity, Tellus, Series B: Chemical and Physical Meteorology, 58, 390–417, https://doi.org/10.1111/j.1600-0889.2006.00223.x, 2006.

Lienert, S. and Joos, F.: A Bayesian ensemble data assimilation to constrain model parameters and land-use carbon emissions, Biogeosciences, 15, 2909–2930, https://doi.org/10.5194/bg-15-2909-2018, https://www.biogeosciences.net/15/2909/2018/, 2018.

Lindgren, A., Hugelius, G., and Kuhry, P.: Extensive loss of past permafrost carbon but a net accumulation into present-day soils, Nature,
30   560, 219–222, https://doi.org/10.1038/s41586-018-0371-0, 2018.

Lloyd, J. and Farquhar, G. D.: 13C discrimination during CO2 assimilation by the terrestrial biosphere, Oecologia, 99, 201–215, https://doi.org/10.1007/BF00627732, 1994.

Lord, N. S., Ridgwell, A., Thorne, M. C., and Lunt, D. J.: An impulse response function for the 'long tail' of excess atmospheric CO2 in an Earth system model, Global Biogeochemical Cycles, https://doi.org/10.1002/2014GB005074.Received, 2015.

35   Lourantou, A., Chappellaz, J., Barnola, J. M., Masson-Delmotte, V., and Raynaud, D.: Changes in atmospheric CO2 and its carbon isotopic ratio during the penultimate deglaciation, Quaternary Science Reviews, 29, 1983–1992, https://doi.org/10.1016/j.quascirev.2010.05.002, http://dx.doi.org/10.1016/j.quascirev.2010.05.002, 2010.

Lüthi, D., Le Floch, M., Bereiter, B., Blunier, T., Barnola, J. M., Siegenthaler, U., Raynaud, D., Jouzel, J., Fischer, H., Kawamura, K., and Stocker, T. F.: High-resolution carbon dioxide concentration record 650,000-800,000 years before present, Nature, 453, 379–382, https://doi.org/10.1038/nature06949, 2008.

Maier-Reimer, E. and Hasselmann, K.: Transport and storage of CO2 in the ocean ——an inorganic ocean-circulation carbon cycle model, Climate Dynamics, 2, 63–90, https://doi.org/10.1007/BF01054491, 1987.

Marcott, S. a., Bauska, T. K., Buizert, C., Steig, E. J., Rosen, J. L., Cuffey, K. M., Fudge, T. J., Severinghaus, J. P., Ahn, J., Kalk, M. L., McConnell, J. R., Sowers, T., Taylor, K. C., White, J. W. C., and Brook, E. J.: Centennial-scale changes in the global carbon cycle during the last deglaciation., Nature, 514, 616–9, https://doi.org/10.1038/nature13799, 2014.

Menviel, L. and Joos, F.: Toward explaining the Holocene carbon dioxide and carbon isotope records: Results from transient ocean carbon cycle-climate simulations, Paleoceanography, 27, 1–17, https://doi.org/10.1029/2011PA002224, 2012.

Menviel, L., Joos, F., and Ritz, S. P.: Simulating atmospheric CO2, 13C and the marine carbon cycle during the Last Glacial-Interglacial cycle: Possible role for a deepening of the mean remineralization depth and an increase in the oceanic nutrient inventory, Quaternary Science Reviews, 56, 46–68, https://doi.org/10.1016/j.quascirev.2012.09.012, 2012.

Menviel, L., Mouchet, A., Meissner, K. J., Joos, F., and England, M. H.: Impact of oceanic circulation changes on atmospheric d13CO2, Global Biogeochemical Cycles, 29, 1944–1961, https://doi.org/10.1002/2015GB005207, 2015.

Mook, W. G.: 13C in Atmospheric CO2, Netherlands Journal of Sea Research, 20, 211–223, 1986.

Müller, S. A., Joos, F., Edwards, N. R., and Stocker, T. F.: Water Mass Distribution and Ventilation Time Scales in a Cost-Efficient, Three-Dimensional Ocean Model, Journal of Climate, 19, 5479–5499, https://doi.org/10.1175/JCLI3911.1, 2006.

Najjar, R. G. and Orr, J. C.: Biotic-HOWTO. Internal OCMIP, Tech. rep., LSCE/CEA, Saclay, Gif-sur-Yvette, France, 1999.

Neftel, A., Oeschger, H., Schwander, J., Stauffer, B., and R, Z.: Ice core sample measurements give atmospheric CO2 content during the past 40,000 yr, Nature, 295, 220–223, 1982.

Oliver, K. I. C., Hoogakker, B. A. A., Crowhurst, S., Henderson, G. M., Rickaby, R. E. M., Edwards, N. R., and Elderfield, H.: A synthesis of marine sediment core d13C data over the last 150 000 years, Climate of the Past, 6, 645–673, https://doi.org/10.5194/cp-6-645-2010, 2010.

Orr, J. C. and Epitalon, J. M.: Improved routines to model the ocean carbonate system: Mocsy 2.0, Geoscientific Model Development, 8, 485–499, https://doi.org/10.5194/gmd-8-485-2015, 2015.

Orr, J. C., Najjar, R., Sabine, C. L., and Joos, F.: Abiotic-HOWTO. Internal OCMIP, Tech. rep., LSCE/CEA, Saclay, Gif-sur-Yvette, France, 1999.

Orr, J. C., Najjar, R. G., Aumont, O., Bopp, L., Bullister, J. L., Danabasoglu, G., Doney, S. C., Dunne, J. P., Dutay, J. C., Graven, H., Griffies, S. M., John, J. G., Joos, F., Levin, I., Lindsay, K., Matear, R. J., McKinley, G. A., Mouchet, A., Oschlies, A., Romanou, A., Schlitzer, R., Tagliabue, A., Tanhua, T., and Yool, A.: Biogeochemical protocols and diagnostics for the CMIP6 Ocean Model Intercomparison Project (OMIP), Geoscientific Model Development, 10, 2169–2199, https://doi.org/10.5194/gmd-10-2169-2017, 2017.

Parekh, P., Joos, F., and Müller, S. A.: A modeling assessment of the interplay between aeolian iron fluxes and iron-binding ligands in controlling carbon dioxide fluctuations during Antarctic warm events, Paleoceanography, 23, 1–14, https://doi.org/10.1029/2007PA001531, 2008.

Revelle, R. and Suess, H. E.: Carbon Dioxide Exchange Between Atmosphere and Ocean and the Question of an Increase of Atmospheric CO2 during the Past Decades, Tellus, 9, 18–27, https://doi.org/10.1111/j.2153-3490.1957.tb01849.x, 1957.

Ridgwell, A. and Hargreaves, J. C.: Regulation of atmospheric CO2 by deep-sea sediments in an Earth system model, Global Biogeochemical
   Cycles, 21, 1–14, https://doi.org/10.1029/2006GB002764, 2007.

Ritz, S., Stocker, T., and Joos, F.: A Coupled Dynamical Ocean-Energy Balance Atmosphere Model for Paleoclimate Studies, Journal of
   Climate, 24, 349–375, https://doi.org/10.1175/2010JCLI3351.1, 2011.

5 Roth, R. and Joos, F.: Model limits on the role of volcanic carbon emissions in regulating glacial-interglacial CO2variations, Earth and
   Planetary Science Letters, 329-330, 141–149, https://doi.org/10.1016/j.epsl.2012.02.019, 2012.

Roth, R., Ritz, S. P., and Joos, F.: Burial-nutrient feedbacks amplify the sensitivity of atmospheric carbon dioxide to changes in organic
   matter remineralisation, Earth System Dynamics, 5, 321–343, https://doi.org/10.5194/esd-5-321-2014, 2014.

Sarmiento, J. L., Orr, J. C., and Siegenthaler, U.: A perturbation simulation of CO2 uptake in an ocean general circulation model, Journal of
10   Geophysical Research: Oceans, 97, 3621–3645, https://doi.org/10.1029/91JC02849, https://agupubs.onlinelibrary.wiley.com/doi/abs/10.
   1029/91JC02849, 1992.

Schimel, D., Alves, D., Enting, I. G., Heimann, M., Joos, F., Raynaud, D., and Wigley, T. M. L.: CO2 and the carbon cycle, in: Climate Change
   1995 The Science of Climate Change Contribution of Working Group I to the Second Assessment Report of the Intergovernmental Panel
   on Climate Change, edited by J. T. Houghton, L. G. Meiro Filho, B. A. Callander, N. Harris, A. K. and Maskell, K., pp. 76–86, Cambridge
15   University Press, 1996.

Schmitt, J., Schneider, R., Elsig, J., Leuenberger, D., Lourantou, a., Chappellaz, J., Kohler, P., Joos, F., Stocker, T. F., Leuen-
   berger, M., and Fischer, H.: Carbon Isotope Constraints on the Deglacial CO2 Rise from Ice Cores, Science, 336, 711–714,
   https://doi.org/10.1126/science.1217161, 2012.

Schneider, R., Schmitt, J., Köhler, P., Joos, F., and Fischer, H.: A reconstruction of atmospheric carbon dioxide and its stable car-
20   bon isotopic composition from the penultimate glacial maximum to the last glacial inception, Climate of the Past, 9, 2507–2523,
   https://doi.org/10.5194/cp-9-2507-2013, 2013.

Siegenthaler, U. and Joos, F.: Use of a simple model for studying oceanic tracer distributions and the global carbon cycle, Tellus B: Chemical
   and Physical Meteorology, 44, 186–207, https://doi.org/10.1034/j.1600-0889.1992.t01-2-00003.x, 1992.

Siegenthaler, U. and Oeschger, H.: Predicting future atmospheric carbon dioxide levels, Science, 199, 388–395,
25   https://doi.org/10.1126/science.199.4327.388, 1978.

Siegenthaler, U., Stocker, T. F., Monnin, E., Lüthi, D., Schwander, J., Stauffer, B., Raynaud, D., Barnola, J.-M., Fischer, H., Masson-Delmotte,
   V., and Jouzel, J.: Stable Carbon Cycle-Climate Relationship During the Late Pleistocene, Science, 310, 1313–1317, 2005.

Sitch, S., Smith, B., Prentice, I. C., Arneth, A., Bondeau, A., Cramer, W., Kaplan, J. O., Levis, S., Lucht, W., Sykes, M. T., Thonicke,
   K., and Venevsky, S.: Evaluation of ecosystem dynamics, plant geography and terrestrial carbon cycling in the LPJ dynamic global
30   vegetation model, Global Change Biology, 9, 161–185, https://doi.org/10.1046/j.1365-2486.2003.00569.x, http://doi.wiley.com/10.1046/
   j.1365-2486.2003.00569.x, 2003.

Skinner, L. C., Fallon, S., Waelbroeck, C., Michel, E., Barker, S., Klug, A., Stark, A., Peters, K., Schnering, H. G., Umemoto, K., Yamaguchi,
   K., Fujita, M., Powers, R. E., Parac, T. N., Raymond, K. N., Olenyuk, B., Muddiman, D. C., Smith, R. D., Whiteford, J. A., Stang, P. J.,
   Levin, M. D., Shield, J. E., Egan, S. J., Robson, R., Dress, A. W. M., Roy, S., Ni, Z., Yaghi, O. M., Lu, J., Mondal, A., Zaworotko, M. J.,
35   Atwood, J. L., Tominaga, M., Kawano, M., Tang, C., Wiesenfeld, K., Gustafson, S., Pelta, D. A., Verdegay, J. L., Systems, B., Pelzing,
   M., Skinner, L. C., Fallon, S., Waelbroeck, C., Michel, E., and Barker, S.: Ventilation of the Deep Southern Ocean and Deglacial CO2
   Rise, Science, 328, 1147–1151, https://doi.org/10.1126/science.1183627, 2010.

Skinner, L. C., Primeau, F., Freeman, E., De La Fuente, M., Goodwin, P. A., Gottschalk, J., Huang, E., McCave, I. N., Noble, T. L., and Scrivner, A. E.: Radiocarbon constraints on the glacial ocean circulation and its impact on atmospheric CO2, Nature Communications, 8, 1–10, https://doi.org/10.1038/ncomms16010, 2017.

Stocker, B. D., Roth, R., Joos, F., Spahni, R., Steinacher, M., Zaehle, S., Bouwman, L., Xu-Ri, and Prentice, I. C.: Multiple

5   greenhouse-gas feedbacks from the land biosphere under future climate change scenarios, Nature Climate Change, 3, 666–672, https://doi.org/10.1038/nclimate1864, http://dx.doi.org/10.1038/nclimate1864, 2013.

Tarnocai, C., Canadell, J. G., Schuur, E. A. G., Kuhry, P., Mazhitova, G., and Zimov, S.: Soil organic carbon pools in the northern circumpolar permafrost region, Global Biogeochemical Cycles, 23, 1–11, https://doi.org/10.1029/2008GB003327, 2009.

Tschumi, T., Joos, F., Gehlen, M., and Heinze, C.: Deep ocean ventilation, carbon isotopes, marine sedimentation and the deglacial CO2 rise,

10   Climate of the Past, 7, 771–800, https://doi.org/10.5194/cp-7-771-2011, 2011.

Wanninkhof, R.: Relationship between wind speed and gas exchange over the ocean, Journal of Geophysical Research, 97, 7373, https://doi.org/10.1029/92JC00188, http://doi.wiley.com/10.1029/92JC00188, 1992.

Wanninkhof, R.: Relationship between wind speed and gas exchange over the ocean revisited, Limnology and Oceanography: Methods, 12, 351–362, https://doi.org/10.4319/lom.2014.12.351, http://doi.wiley.com/10.4319/lom.2014.12.351, 2014.